

Combined carbon, hydrogen, and clumped isotope fractionations reveal differential reversibility of hydrogenotrophic methanogenesis in laboratory cultures

Jeemin H. Rhim¹ and Shuhei Ono²

¹Dartmouth College

²Massachusetts Institute of Technology

November 22, 2022

Abstract

Stable isotope analysis has been widely used to aid the source identification of methane. However, the isotopic ($^{13}\text{C}/^{12}\text{C}$ and D/H) and isotopologue ($^{13}\text{CH}_3\text{D}$ and $^{12}\text{CH}_2\text{D}_2$) signatures of microbial methane in natural environments are often different from those in laboratory cultures in which methanogens are typically grown under optimal conditions. Growth phase and hydrogen (H_2) concentration have been proposed as factors controlling the isotopic compositions of methane, but their effects on the relationship among carbon, hydrogen and doubly-substituted “clumped” isotopologue systems have not been assessed in a quantitative framework. Here we experimentally investigate the bulk ($\delta^{13}\text{C}$ and δD) and clumped ($[\delta^{13}\text{CH}_3\text{D}]$) isotopologue compositions of methane produced by hyperthermophilic hydrogenotrophic (CO_2 -reducing) methanogens using batch and fed-batch systems at different growth phases and H_2 mixing ratios (*Methanocaldococcus bathoardescens* at 82 or 60 °C and on 80 or 25% H_2 ; *Methanothermobacter thermautotrophicus* [$\delta^2\text{H}$] at 65 degC and on 20, 5 or 1.6% H_2). We observed a large range (18 to 63‰) carbon isotope fractionations, with larger values observed during later growth phase, consistent with previous observations. In contrast, hydrogen isotope fractionations remained relatively constant at -31.7 ± 2.5 ‰ suggesting that dissolution of gaseous H_2 into liquid media became the rate limit as cell density increased. Accordingly, the low (and undersaturated) dissolved H_2 concentrations can explain the increased carbon isotope fractionations during the later growth phase. The δD and $\Delta^{13}\text{CH}_3\text{D}$ values indicated departure from equilibrium throughout experiments. As the cell density increased and dissolved H_2 decreased, $\Delta^{13}\text{CH}_3\text{D}$ decreased (further departure from equilibrium), contrary to expectations from previous models. Our isotopologue flow network model reproduced the observed trends when the last H-addition step is less reversible relative to the first three H-addition steps (up to $\text{CH}_3\text{-CoM}$). In this differential reversibility model, carbon, hydrogen and clumped isotopologue fractionations are largely controlled by the reversibility of the first three H-addition steps under high H_2 concentrations; the last H-addition step becomes important under low H_2 . The magnitude of depletion and decreasing trend in $\Delta^{13}\text{CH}_3\text{D}$ values were reproduced when a large ($\delta^2\text{H}$) model. This study highlights the advantage of combined bulk and clumped isotope analyses and the importance of physiological factors (growth phase) and energy availability (dissolved H_2 concentration) when using isotope analyses to aid the source identification of methane.

1 Combined carbon, hydrogen, and clumped isotope fractionations reveal differential
2 reversibility of hydrogenotrophic methanogenesis in laboratory cultures

3
4 Jeemin H. Rhim^{a,1,*} and Shuhei Ono^a

5
6 ^a Department of Earth, Atmospheric and Planetary Sciences, Massachusetts Institute of Technology, Cambridge, MA 02139,
7 USA. jrhim@alum.mit.edu (J. H. Rhim), sono@mit.edu (S. Ono)

8 ¹ Present address: Department of Earth Sciences, Dartmouth College, Hanover, NH 03755, USA

9 * Corresponding author: jrhim@alum.mit.edu

10
11 **Abstract**

12
13 Stable isotope analysis has been widely used to aid the source identification of methane. However,
14 the isotopic (¹³C/¹²C and D/H) and isotopologue (¹³CH₃D and ¹²CH₂D₂) signatures of microbial
15 methane in natural environments are often different from those in laboratory cultures in which
16 methanogens are typically grown under optimal conditions. Growth phase and hydrogen (H₂)
17 concentration have been proposed as factors controlling the isotopic compositions of methane, but
18 their effects on the relationship among carbon, hydrogen and doubly-substituted “clumped”
19 isotopologue systems have not been assessed in a quantitative framework. Here we experimentally
20 investigate the bulk (δ¹³C and δD) and clumped (Δ¹³CH₃D) isotopologue compositions of methane
21 produced by hyperthermophilic hydrogenotrophic (CO₂-reducing) methanogens using batch and
22 fed-batch systems at different growth phases and H₂ mixing ratios (*Methanocaldococcus*
23 *bathoardescens* at 82 or 60 °C and on 80 or 25% H₂; *Methanothermobacter thermautotrophicus*
24 ΔH at 65 °C and on 20, 5 or 1.6% H₂). We observed a large range (18 to 63‰) of carbon isotope
25 fractionations, with larger values observed during later growth phase, consistent with previous
26 observations. In contrast, hydrogen isotope fractionations remained relatively constant at -317 ±
27 25‰. Linear growth was observed for experiments with *M. bathoardescens*, suggesting that
28 dissolution of gaseous H₂ into liquid media became the rate limit as cell density increased.
29 Accordingly, the low (and undersaturated) dissolved H₂ concentrations can explain the increased
30 carbon isotope fractionations during the later growth phase. The δD and Δ¹³CH₃D values indicated
31 departure from equilibrium throughout experiments. As the cell density increased and dissolved
32 H₂ decreased, Δ¹³CH₃D decreased (further departure from equilibrium), contrary to expectations
33 from previous models. Our isotopologue flow network model reproduced the observed trends
34 when the last H-addition step is less reversible relative to the first three H-addition steps (up to
35 CH₃-CoM). In this differential reversibility model, carbon, hydrogen and clumped isotopologue
36 fractionations are largely controlled by the reversibility of the first three H-addition steps under
37 high H₂ concentrations; the last H-addition step becomes important under low H₂. The magnitude
38 of depletion and decreasing trend in Δ¹³CH₃D values were reproduced when a large (≥6‰)
39 secondary clumped kinetic isotope effect was considered in the model. This study highlights the
40 advantage of combined bulk and clumped isotope analyses and the importance of physiological
41 factors (growth phase) and energy availability (dissolved H₂ concentration) when using isotope
42 analyses to aid the source identification of methane.

43 1 Introduction

44 Methane (CH₄) is an important energy source, a potent greenhouse gas as well as a potential
45 biosignature in subsurface and extraterrestrial environments. Stable carbon ($\delta^{13}\text{C}$) and hydrogen
46 (δD) isotope ratios have been extensively used to apportion the relative contributions of different
47 methanogenic pathways, e.g., acetoclastic *vs.* hydrogenotrophic methanogenesis (Welhan and
48 Lupton, 1987; Whiticar, 1990; Sherwood Lollar et al., 2002; Flores et al., 2008; Sherwood Lollar
49 et al., 2008; Pohlman et al., 2009; Baldassare et al., 2014). More recently, technological advances
50 have allowed the precise measurements of the abundance of multiply-substituted or “clumped”
51 isotopologues of methane (e.g., ¹³CH₃D and ¹²CH₂D₂; Ono et al., 2014; Stolper et al., 2014; Young
52 et al., 2016; Gonzalez et al., 2019). Methane clumped isotopologue abundance has in some cases
53 served as an isotopic geothermometer and provided temperature estimates that are consistent with
54 environmental temperatures (e.g., Stolper et al., 2015; Wang et al., 2015; Young et al., 2017).

55 While both bulk and clumped isotopic compositions of methane can help identify the
56 source(s) of methane, some factors complicate the interpretation of the isotopic signatures. For
57 example, overlapping isotopic signatures in $\delta^{13}\text{C}$ and δD often lead to ambiguous source
58 identifications (e.g., Schoell, 1988; Whiticar, 1990, 1999; Pohlman et al., 2009; Etiope and
59 Sherwood Lollar, 2013), and some microbial methane samples from surface environments have
60 yielded unreasonably high temperature estimates for clumped isotopologue equilibrium (e.g.,
61 Stolper et al., 2015; Wang et al., 2015; Douglas et al., 2017; Young et al., 2017). In particular,
62 there are significant discrepancies between the bulk and clumped isotopic signatures observed in
63 natural samples of microbial methane and those produced by laboratory cultures that presumably
64 use the same metabolic pathway (Stolper et al., 2015; Wang et al., 2015; Okumura et al., 2016;
65 Young et al., 2017; Gruen et al., 2018). In general, the $\delta^{13}\text{C}$ and δD values of microbial methane

66 in marine environments, where hydrogenotrophic methanogenesis is thought to be a primary
67 methanogenic pathway, tend to indicate isotopic equilibrium with CO₂ and H₂O. In contrast, the
68 δ¹³C and δD values observed in laboratory cultures often indicate kinetic isotope effect (i.e.,
69 departure from equilibrium). Similarly, the Δ¹³CH₃D values, representing the relative abundance
70 of ¹³CH₃D clumped isotopologues, measured from microbial methane in marine and deep
71 subsurface sediments indicate internal isotopic equilibrium whereas those from pure cultures carry
72 strong kinetic isotope signatures (Stolper et al., 2015; Wang et al., 2015; Douglas et al., 2017;
73 Young et al., 2017; Gruen et al., 2018).

74 Previous studies that investigated the factors controlling isotope fractionation during
75 microbial methanogenesis shed some light on the cause of the observed discrepancy. Multiple
76 studies have investigated the changes in the carbon isotope fractionation factor (¹³α) during
77 hydrogenotrophic methanogenesis and have identified growth phase and/or hydrogen partial
78 pressure (*p*H₂) as important controlling factors (Games and Hayes, 1978; Fuchs et al., 1979a;
79 Belyaev et al., 1983; Balabane et al., 1987; Krzycki et al., 1987; Botz et al., 1996; Valentine et al.,
80 2004; Penning et al., 2005; Londry et al., 2008; Yoshioka et al., 2008; Hattori et al., 2012;
81 Okumura et al., 2016; Topçuoğlu et al., 2019; Nguyen et al., 2020). In general, carbon isotope
82 fractionation increases at low *p*H₂ such that the apparent magnitude of fractionation is close to that
83 expected at CH₄-CO₂ equilibrium. These observations corroborate the differential reversibility
84 hypothesis, which predicts that the variation in carbon isotope fractionation is a result of the
85 changes in reversibility in the enzymatic steps of the hydrogenotrophic methanogenesis pathway
86 (Valentine et al., 2004).

87 The effect of *p*H₂ on hydrogen isotope fractionation has been investigated by comparing
88 pure cultures grown on high concentrations of H₂ against cocultures containing hydrogenotrophic

89 methanogens and syntrophic heterotrophic bacteria (e.g., *Syntrophothermus lipocalidus* str. TGB-
90 C1 and *Methanothermobacter thermautotrophicus* str. Δ H) (Yoshioka et al., 2008; Hattori et al.,
91 2012; Okumura et al., 2016). Cocultures provide a means to create relatively low H_2 conditions
92 (e.g., 6.8 to 64.9 Pa; Okumura et al., 2016) compared to high pH_2 conditions ($>10^5$ Pa) often used
93 for pure cultures grown on H_2 . So far, to the best of our knowledge, no experiment has observed
94 the magnitude of hydrogen isotope fractionation expected at CH_4 - H_2O equilibrium (ca. -178% at
95 $25\text{ }^\circ\text{C}$; Horita and Wesolowski, 1994; Gropp, Iron and Halevy, 2021) that is often observed in
96 natural samples of microbial methane. If the differential reversibility hypothesis can be applied to
97 hydrogen isotope system, higher reversibility and near-equilibrium hydrogen isotope fractionation
98 are expected at lower H_2 environments. This would suggest that the H_2 concentrations tested in
99 experiments so far were not low enough to produce near-equilibrium hydrogen isotope signatures.

100 Laboratory experiments with methane clumped isotope data have only been conducted in
101 batch cultures under high pH_2 conditions (e.g., Stolper et al., 2015; Wang et al., 2015; Young et
102 al., 2017; Gruen et al., 2018). Isotope models relating the dissolved H_2 concentration and $\Delta^{13}CH_3D$
103 values have been proposed and predict changes in $\Delta^{13}CH_3D$ values toward equilibrium (i.e.,
104 increase in $\Delta^{13}CH_3D$ values toward 6% at $25\text{ }^\circ\text{C}$) at low H_2 concentrations (e.g., Stolper et al.,
105 2015; Wang et al., 2015), consistent with the overall concept of the differential reversibility
106 hypothesis. However, direct investigations of $\Delta^{13}CH_3D$ values produced at different growth phases
107 or H_2 concentrations are needed to validate whether the differential reversibility model can be
108 applied to clumped isotopologue systematics.

109 In this study, we cultured two different species of methanogens, *Methanocaldococcus*
110 *bathoardescens* and *Methanothermobacter thermautotrophicus* str. Δ H, in batch and fed-batch
111 systems under a pH_2 range from 1.6 kPa to 80 kPa and simultaneously measured $\delta^{13}C$ and δD of

112 the substrates (CO₂ and H₂O) as well as the δ¹³C, δD and Δ¹³CH₃D of the product (CH₄). We
113 present isotopologue flow network model results along with the estimated dissolved H₂
114 concentrations and measured isotopologue ratios to explain the observed fractionation trends by
115 the effects of differential reversibility at the last H-addition step. We propose the δ¹³C, δD and
116 Δ¹³CH₃D trajectories expected for a wide range of dissolved H₂ concentrations encompassing both
117 natural environments and experimental conditions (10⁻⁹ to 10⁻² M H₂) that can be applied for future
118 investigations of these isotope signatures for source identifications of methane.

119 **2 Materials and Methods**

120 2.1 Organisms

121 Cultures of *Methanocaldococcus bathoardescens* were provided by James F. Holden (University
122 of Massachusetts, Amherst). Culture medium for *M. bathoardescens* was prepared following the
123 “282 mod” recipe (Ver Eecke *et al.*, 2012) containing (L⁻¹): 0.34 g KCl, 4.00 g MgCl₂·6H₂O, 0.14
124 g KH₂PO₄, 3.45 g MgSO₄·7H₂O, 18 g NaCl, 0.25 g NH₄Cl, 0.14 g CaCl₂·2H₂O, 2.0 mL
125 Fe(NH₄)₂(SO₄)₂·6H₂O (0.1% w/v), 10.0 mL trace element solution SL-10 (DSMZ 320), 5.00 g
126 NaHCO₃, 10.0 mL vitamins solution (DSMZ 141). Resazurin was omitted, and 2 mM cysteine and
127 1 mM sulfide were used as reducing agents instead of dithiothreitol.

128 *Methanothermobacter thermautotrophicus* str ΔH (DSMZ 1053) was purchased from the
129 German Collection of Microorganisms and Cell Cultures (DSMZ, Braunschweig, Germany). The
130 seed culture was transferred to and maintained in mineral medium modified from DSMZ 1523
131 containing (L⁻¹): 0.50 g KH₂PO₄, 0.40 g MgSO₄·7H₂O, 0.40 g NaCl, 0.40 g NH₄Cl, 0.05 g
132 CaCl₂·2H₂O, 1.00 mL trace element solution SL-10 (DSMZ 320), 4.00 g NaHCO₃, 1.00 mL
133 vitamins solution (DSMZ 503). The medium was reduced with 1 mM sulfide.

134 2.2 Culture conditions

135 Table 1 summarizes the conditions for culture experiments conducted in this study. *M.*
136 *bathoardescens* was grown at 82 or 60 °C and on 80 or 25% H₂, and *M. thermotrophicus* ΔH
137 was grown at 65 °C and on 20, 5 or 1.6% H₂.

138 2.2.1 Batch cultures

139 *M. bathoardescens* batch culture series was prepared in 100 mL of “282mod” medium described
140 above in 200 mL bottles with 2 bars absolute pressure of H₂/CO₂ (80:20). Each bottle was
141 inoculated with 2% (v/v) of pre-culture in exponential growth phase. Cultures were incubated at
142 82 °C. At given timepoints, culture headspace was sampled for gas chromatography and δ¹³C_{CO2}
143 analysis. Medium was sampled for cell counts with a counting chamber (CTL-HEMM-GLDR,
144 LW Scientific; depth = 0.1 mm) and phase-contrast light microscope. Immediately after sampling,
145 the entire remaining culture was sacrificed by adding 5 mL of 1 M sodium hydroxide. The
146 headspace of a killed culture was used for methane purification and subsequent isotopologue
147 analysis.

148 2.2.2 Fed-batch cultures

149 All fed-batch culturing experiments were carried out using a 2-L glass bioreactor (Ace Glass)
150 equipped with a fritted gas dispersion tube (Ace Glass), pH meter (ML-05990-40; Cole-Parmer),
151 temperature monitor/controller, liquid sampling port and a condenser leading to the gas outlet
152 (Figure 1). Both the culturing apparatus and 1.7 L of medium were sterilized by autoclaving at
153 121 °C for 20 minutes. A set of mass flow controllers was used to control the flow rates of H₂,
154 CO₂ and He (or N₂) to achieve desired mixing ratios of H₂, xH₂, (80, 25, 20, 5 and 1.6%) in the
155 influent gas (Table 1). A column filled with copper was placed between the gas tanks and the

156 reactor and heated to 450 °C to remove trace amounts of oxygen in the incoming gas mixture
157 (Wolfe, 2011). After the reactor was heated to desired temperatures (82, 65 or 60 °C), vitamin
158 solution was added and the pH was adjusted to 6.0 and 7.0 (for *M. bathoardescens* and *M.*
159 *thermautotrophicus*, respectively) while bubbling with the gas mixture (20% CO₂). Cysteine (2
160 mM) and sulfide (2 mM) or cysteine (2 mM) and titanium citrate (0.1 mM) were added as reducing
161 agents before adding a 2% (v/v) of inoculum. Effluent gas from the reactor was passed through a
162 condenser (12 °C) which is followed by an additional column filled with CaCl₂ for water removal,
163 and directly connected to an on-line gas chromatography system or a gas sampling bag (Cali-5-
164 Bond™, Calibrated Instruments, Inc., McHenry, MD, USA) (Figure 1).

165 2.3 Analytical procedures

166 2.3.1 Gas chromatography

167 Mixing ratios of headspace gases were measured using a gas chromatograph (GC-2014, Shimadzu,
168 Columbia, MD, USA), equipped with a packed column (Carboxen-1000, 5' by 1/8", Supelco,
169 Bellefonte, PA, USA) with argon carrier gas at 140 °C. A thermal conductivity and a methanizer-
170 flame ionization detector were used to quantify the mixing ratios of H₂, N₂, CH₄ and CO₂. The
171 following compositions of commercial and in-house standard gases were used for calibration: 7%
172 CO, 15% CO₂, 4% O₂, 4.5% CH₄ balanced in N₂ (Supelco; P/N 501743); 4% CH₄, 20% CO₂, 2%
173 CO balanced in N₂ (MESA International Technologies, Inc.); 80% H₂, 20% CO₂ (Airgas). The
174 accuracy of GC analyses was ±5% of measured values. Headspace samples from experiments B.82
175 and F.82.80 were analyzed via manual syringe injection, and all other experiments were measured
176 on-line GC using a gas sampling valve with a 500µL injection loop (VC-SL500CW, VICI Valco,
177 Houston, TX, USA) (Figure 1).

178 2.3.2 $\delta^{13}\text{C}_{\text{CO}_2}$ analysis

179 The carbon isotopic composition of headspace CO_2 ($\delta^{13}\text{C}_{\text{CO}_2}$) was measured using an isotope-ratio
180 mass spectrometer (IRMS; MAT 253, Thermo-Fisher). CO_2 from subsamples of the headspace gas
181 collected from serum bottles (batch cultures) or at the exhaust (fed-batch cultures) was purified by
182 cryogenically separating water and CO_2 from H_2 , N_2 and CH_4 into a cold trap at $-196\text{ }^\circ\text{C}$ and
183 warming up the trap to $-80\text{ }^\circ\text{C}$ and freezing the eluted CO_2 in a sample vial. Typical analytical
184 precision for $\delta^{13}\text{C}$ analysis is $\pm 0.2\text{‰}$.

185 2.3.3 $\delta\text{D}_{\text{H}_2\text{O}}$ analysis

186 The hydrogen isotopic composition of media water ($\delta\text{D}_{\text{H}_2\text{O}}$) was measured using cavity ring-down
187 spectrometry (L-1102i WS-CRDS, Picarro, Sunnyvale, CA, USA) at the University of
188 Massachusetts Amherst. Samples were vaporized at $110\text{ }^\circ\text{C}$. International reference standards
189 (IAEA, Vienna, Austria) were used to calibrate the instrument to the VSMOW-VSLAP scale and
190 working standards were used with each analytical run. Long-term averages of internal laboratory
191 standard analytical results yield an instrumental precision of 0.5‰ .

192 2.3.4 Methane isotopologue analysis

193 Methane samples were purified following the preparative GC method described by Wang et al.
194 (2015). For batch culture experiment (B.82), the entire headspace of each killed serum bottle was
195 replaced with helium during the sample preparation. For fed-batch experiments, multi-layer foil
196 sampling bags (Cali-5-BondTM, Calibrated Instruments, Inc., McHenry, MD, USA) used to collect
197 downstream headspace gas at the exhaust were directly connected to the sample preparation system.
198 The relative abundances of methane isotopologues $^{12}\text{CH}_4$, $^{13}\text{CH}_4$, $^{12}\text{CH}_3\text{D}$ and $^{13}\text{CH}_3\text{D}$ were

199 measured using a tunable infrared laser direct absorption spectroscopy (TILDAS) described
200 previously (Ono et al., 2014; Wang et al., 2015).

201 2.3.5 Isotope notation and calculation of isotope fractionation factors

202 Bulk isotope values are reported using standard delta notation:

$$\delta^{13}\text{C} = \frac{(^{13}\text{C}/^{12}\text{C})_{\text{sample}}}{(^{13}\text{C}/^{12}\text{C})_{\text{VPDB}}} - 1 \quad (\text{Eqn. 1})$$

$$\delta\text{D} = \frac{(\text{D}/\text{H})_{\text{sample}}}{(\text{D}/\text{H})_{\text{VSMOW}}} - 1 \quad (\text{Eqn. 2})$$

203 where VPDB and VSMOW are Vienna Pee Dee Belemnite and Vienna Standard Mean Ocean
204 Water, respectively. The factor of 1000 was omitted from (Eqn. 1) and (Eqn. 2), following the
205 IUPAC recommendations (Coplen, 2011). Natural gas samples with published $\delta^{13}\text{C}$ and δD values
206 (NGS-1 and NGS-3) were used for the calibration of $\delta^{13}\text{C}$ and δD values of methane analyzed via
207 TILDAS (Wang et al., 2015). Experimental samples were considered to contain methane
208 isotopologues at or sufficiently close to their natural abundances, hence the following
209 approximations are valid within analytical uncertainty: $^{13}\text{C}/^{12}\text{C} \approx [^{13}\text{CH}_4]/[^{12}\text{CH}_4]$ and $\text{D}/\text{H} \approx \frac{1}{4}$
210 $[^{12}\text{CH}_3\text{D}]/[^{12}\text{CH}_4]$. The abundance of $^{13}\text{CH}_3\text{D}$ clumped isotopologue is reported as $\Delta^{13}\text{CH}_3\text{D}$, a
211 metric representing the deviation of the abundance of $^{13}\text{CH}_3\text{D}$ from a random distribution of
212 isotopes among isotopologues $^{12}\text{CH}_4$, $^{13}\text{CH}_4$, $^{12}\text{CH}_3\text{D}$ and $^{13}\text{CH}_3\text{D}$ (Ono et al., 2014; Wang et al.,
213 2015):

$$\Delta^{13}\text{CH}_3\text{D} = \frac{[^{13}\text{CH}_3\text{D}][^{12}\text{CH}_4]}{[^{13}\text{CH}_4][^{12}\text{CH}_3\text{D}]} - 1 \quad (\text{Eqn. 3})$$

214 The value of $\Delta^{13}\text{CH}_3\text{D}$ was calibrated by equilibrating methane at 250 °C using Pt catalyst (Ono
215 et al., 2014).

216 The isotope fractionation factor (α) is defined as the ratio of relative abundances of isotopes
217 between a substrate and its product. For a batch experiment (B.82), isotope fractionation factors
218 are calculated assuming an irreversible closed system isotope effect, based on the conventional
219 Rayleigh equation (Mariotti et al., 1981). For the reduction of CO_2 to CH_4 :

$$({}^{13}\alpha - 1) \cdot \ln f = \ln \frac{\delta^{13}\text{C} + 1}{\delta^{13}\text{C}_0 + 1} \quad (\text{Eqn. 4})$$

220 where f is the fraction of CO_2 remaining; ${}^{13}\alpha$ is the kinetic isotope fractionation factor for ${}^{13}\text{C}/{}^{12}\text{C}$;
221 and $\delta^{13}\text{C}_0$ is the initial isotopic compositions of CO_2 .

222 The bulk isotope fractionation factors for fed-batch experiments (F.82.80, F.60.80, F.82.25,
223 F.65.20 and F.65.5) were calculated as follows:

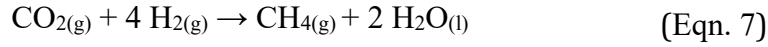
$${}^{13}\alpha_{\text{CH}_4/\text{CO}_2} = \frac{\delta^{13}\text{C}_{\text{CH}_4} + 1}{\delta^{13}\text{C}_{\text{CO}_2} + 1} \quad (\text{Eqn. 5})$$

$${}^2\alpha_{\text{CH}_4/\text{H}_2\text{O}} = \frac{\delta\text{D}_{\text{CH}_4} + 1}{\delta\text{D}_{\text{H}_2\text{O}} + 1} \quad (\text{Eqn. 6})$$

224 The equilibrium fractionation factors for carbon (${}^{13}\alpha_{\text{eq}}$; Horita, 2001), hydrogen (${}^2\alpha_{\text{eq}}$; Horibe and
225 Craig, 1995) and clumped ($\Delta^{13}\text{CH}_3\text{D}_{\text{eq}}$; Ono et al., 2014) isotope systems were calculated based
226 on experimental and/or theoretical calibrations.

227 2.3.6 Data processing

228 Methanogenesis reaction,



229 consumes 5 molecules of gas and produce 1 molecule of gas and water that is mostly in liquid
 230 phase. Because of this decrease in volume, the flow rate of effluent gas (Q_{out}) does not equal to the
 231 flow rate of the influent gas (Q_{in} : 200 mL/min) and can be lower by up to 25% for our experimental
 232 conditions. Based on the stoichiometry of the reaction (Eqn. 7), the flow rate of effluent gas was
 233 calculated from the mixing ratios of H_2 and CH_4 :

$$Q_{\text{out}} = \frac{x_{\text{H}_2}^{\text{in}}}{4x_{\text{CH}_4}^{\text{out}} + x_{\text{H}_2}^{\text{out}}} \cdot Q_{\text{in}} \quad (\text{Eqn. 8})$$

234 where $x_{\text{H}_2}^{\text{in}}$ and $x_{\text{H}_2}^{\text{out}}$ are H_2 mixing ratios of the influent and effluent gases, respectively, and $x_{\text{CH}_4}^{\text{out}}$
 235 is CH_4 mixing ratio of the effluent gas measured by the GC.

236 The total methane production rate (MPR ; mol/hr) was calculated from GC measurements
 237 of $x_{\text{CH}_4}^{\text{out}}$ and Q_{out} calculated above:

$$MPR = \frac{P}{RT} \cdot Q_{\text{out}} \cdot x_{\text{CH}_4}^{\text{out}} \quad (\text{Eqn. 9})$$

238 where R is gas constant ($8.314 \text{ m}^3 \cdot \text{Pa} / \text{mol} \cdot \text{K}$), and T and P are temperature (K) and headspace
 239 pressure ($\approx 10^5 \text{ Pa}$) during measurements. Cell-specific MPR (csMPR ; mol/cell/hr) was calculated
 240 by dividing MPR by the total number of cells in the reactor:

$$\text{csMPR} = \frac{MPR}{N_c \cdot V_{\text{liq}}} \quad (\text{Eqn. 10})$$

241 where N_c is cell density (cells/ m^3), V_{liq} is the volume of media (m^3).

242 2.3.7 Estimating dissolved H_2 concentrations in the liquid medium

243 For our experiments, the concentration of dissolved H_2 , $[\text{H}_2]$, is lower than what is expected from
 244 the saturation gas solubility and $p\text{H}_2$ in the influent gas. This is because of 1) high water vapor

245 pressure in the reactor headspace during hyperthermophilic experiments and 2) the slow kinetics
246 of H₂ dissolution from gas phase to liquid media. We considered the following to estimate [H₂].

247 Water vapor pressure at saturation ($p_{\text{H}_2\text{O}_{\text{sat}}}$) can be as high as 0.51 bars at 82 °C, 0.25 bars
248 at 65 °C, and 0.20 bars at 60 °C (Haynes et al., 2016). If headspace gas was saturated with water
249 vapor, p_{H_2} in the gas headspace for our fed-batch reactor can be lower by a factor of two compared
250 to dry gas mixing ratios measured by GC. To consider the water vapor pressure in headspace (and
251 bubbles), we estimated the $p_{\text{H}_2\text{O}}$ -corrected $p_{\text{H}_2,\text{VP}}$ as:

$$p_{\text{H}_2,\text{VP}} = x_{\text{H}_2} \cdot (p_{\text{reactor}} - p_{\text{H}_2\text{O}_{\text{sat}}}) \quad (\text{Eqn. 11})$$

252 where p_{reactor} is the total pressure of reactor, $p_{\text{H}_2\text{O}_{\text{sat}}}$ is the saturation water vapor pressure
253 calculated as a function of temperature. The total pressure of reactor was assumed to be 1 bar.
254 Headspace pressures were measured without inoculation and did not exceed over 1.05 bars.

255 In addition, the mass transport limit of H₂ from gas to dissolved phases can result in
256 significant discrepancies between actual [H₂] and the [H₂] values expected at saturation with the
257 gas phase H₂ (e.g., Pauss et al., 1990; Jud et al., 1997). The mass balance of H₂ for the liquid phase
258 can be expressed as:

$$\frac{d[\text{H}_2]}{dt} = -(\text{H}_2 \text{ consumption rate}) + k_L a \cdot (K_{\text{H}} p_{\text{H}_2,\text{VP}} - [\text{H}_2]) \quad (\text{Eqn. 12})$$

259 where H₂ consumption rate is 4 times the *MPR*, and $k_L a$ is the global mass transfer coefficient (e.g.,
260 hr⁻¹), which quantifies the rate of mass transfer for the whole reactor under a specific experimental
261 condition. K_{H} is the Henry's law constant for H₂ (mol/L/Pa), calculated as a function of
262 temperature and salinity following Chabab et al. (2020). The steady state solution for (Eqn. 12) is:
263

$$[H_2] = K_H \cdot pH_{2,VP} - \frac{4 \cdot MPR}{k_L a} \quad (\text{Eqn. 13})$$

264 The values of $k_L a$ were estimated based on the following equation:

$$k_L a = \frac{D}{\delta \cdot V_{liq}} \cdot a \quad (\text{Eqn. 14})$$

265 where D is the diffusivity coefficient for H_2 (m^2/hr); a is the sum of the surface area at the
 266 headspace-medium interface (A_h) and total surface area of bubbles (A_b) (m^2); and δ is the thickness
 267 of the diffusion layer (m). Using the δ values of $1 \mu m$ and $0.5 \mu m$ and other parameters specific to
 268 the experimental setup of this study (Table 2), $k_L a$ values of 380 and 760 hr^{-1} were used in (Eqn.
 269 13) to calculate $[H_2]$. The parameter $k_L a$ is unique to a specific experimental condition and
 270 therefore varies between studies; however, the $k_L a$ range of 380 to 760 hr^{-1} falls reasonably within
 271 the ranges reported previously (e.g., 0.16 h^{-1} , Pauss et al., 1990; $220\text{--}1540 \text{ h}^{-1}$, Jud et al., 1997).

272 Following are brief justifications of the values used in Table 2. D is a typical diffusion
 273 coefficient for H_2 at $25 \text{ }^\circ\text{C}$, $5.0 \times 10^{-5} \text{ cm}^2 \text{ sec}^{-1}$ (Macpherson and Unwin, 1997). A_b is a function of
 274 the geometry and the number of bubbles, which is determined by the relationship between the size
 275 and residence time of bubbles and Q_{gas} . The upward velocity of bubbles for small bubbles (radius
 276 $< 0.1 \text{ cm}$) was calculated following Park et al. (2017). The residence time and total volume of
 277 bubbles can be calculated for a known travel distance (i.e., height of the medium) and, from this,
 278 the total area of bubbles, A_b , was calculated. Finally, the surface area at the headspace-medium
 279 interface (A_h) is calculated from the reactor dimension.

280 2.3.8 Isotopologue flow network model

281 To examine the isotopologue data in this study with respect to the modeled $[H_2]$ values, we applied
282 the isotopologue flow network model adapted from Wang et al. (2015). The model calculates the
283 expected isotopologue compositions of CH_4 as well as the intermediate carbon-containing species.
284 During hydrogenotrophic methanogenesis (Eqn. 7), CO_2 is reduced to CH_4 via seven reactions and
285 six intermediate carbon species. Following Wang et al. (2015) and Cao et al. (2019), we reduced
286 the number of intermediate species to three by treating species with the same redox state as the
287 same pool (Figure 2A). Two sets of input parameters required for the model are reversibilities (ϕ)
288 for enzymatic reactions in the methanogenesis pathway and kinetic isotope effect (KIE) intrinsic
289 to enzymatic reactions.

290 The first set of input parameters, metabolic reversibility (ϕ), is the ratio of backward to
291 forward fluxes for an enzymatically-mediated reaction (Rees, 1973; Hayes, 2001). Previous
292 models have used a range of ϕ values between 0 and 1, where $\phi = 0$ is fully kinetic (non-
293 equilibrium) and $\phi = 1$ is fully reversible (equilibrium). Stolper et al., (2015) assumed $\phi = 1$ for all
294 except for the last H-addition step, which was varied. Wang et al. (2015) implemented a gradual
295 and uniform departure from equilibrium ($\phi = 1 \rightarrow 0$) for all H-addition steps. Cao et al. (2019)
296 tested binary cases, where ϕ is either 0 or 1 for each H-addition step. More recently, Gropp et al.
297 (2021) re-evaluated these three models with calculated equilibrium fractionation factors and
298 concluded that models in Wang et al. (2015) and Cao et al. (2019) can produce a range of carbon
299 isotope fractionation observed in the natural environment with certain combinations of ϕ . This
300 highlights the importance of ϕ , both in its degree of equilibrium at a given step and in its overall
301 variation among the four H-addition steps, in determining the outputs of isotopologue flow
302 network models. In this work, we parameterized ϕ values for the four H-addition steps as a function
303 of H_2 by assuming Michaelis–Menten kinetics, as described in Wang et al. (2015):

$$\varphi_n = 1 - \frac{[\text{H}_2]}{K_m + [\text{H}_2]} \quad (\text{Eqn. 15})$$

304 where $n=1$ to 4, representing the four H-addition steps (Figure 2A), and K_m is the effective half-
305 saturation constant. According to the model for the energy conservation of hydrogenotrophic
306 methanogenesis, the last step (reduction of methyl-CoM to CH_4) is exergonic and expected to be
307 less reversible compared to other steps (Thauer *et al.*, 2008; Thauer, 2011; Ono *et al.*, *in revision*).

308 We modeled differential reversibility by changing the K_m values (Eqn. 15) and compared
309 the following three cases:

- 310 1) equilibrium end-member scenario with a high K_m value of 10^4 M for all four reactions,
- 311 2) uniform reversibility scenario with a K_m value of 5×10^{-5} M for all four reactions, and
- 312 3) differential reversibility scenario with a K_m value of 5×10^{-5} M for the first three reactions
313 and a K_m value of 10^{-8} M (less reversible) for the last reaction.

314 The K_m value of 5×10^{-5} M approximates the experimentally determined K_m values for
315 hyperthermophilic methanogens (66 μM for three *Methanocaldococcus* species; Ver Eecke *et al.*,
316 2012). The lower K_m value of 10^{-8} M makes the last reversible step largely unidirectional down to
317 a low $[\text{H}_2]$ of $\sim 10^{-8}$ M. For reference, the minimum threshold $p\text{H}_2$ estimated for pure cultures is
318 6.5 Pa (*ca.* 5×10^{-8} M at 25 °C), and the theoretical $p\text{H}_2$ at thermodynamic equilibrium for
319 hydrogenotrophic methanogenesis is 0.1 Pa (*ca.* 1×10^{-9} M at 25 °C) assuming $[\text{CO}_2]/[\text{CH}_4] = 1$
320 (Lovley, 1985; Thauer *et al.*, 2008).

321 The values of KIEs are the second set of required input parameters for the model. KIEs are
322 experimentally determined only for the last reaction catalyzed by methyl-coenzyme M reductase
323 (Scheller *et al.*, 2013). KIEs for other reactions are chosen to reproduce the kinetic end-member
324 solution and maintain the consistency with equilibrium fractionations (Appendix A; Table S1).
325 Equilibrium fractionation factors (α^{eq}) estimated by quantum mechanical calculation (Gropp *et al.*,

2021; Ono et al., 2021) constrain the model solution for the equilibrium end-member scenario (Figure 2B). We use α^{eq} values estimated at 82 °C (experimental temperature for B.82 and F.82.80) by Gropp et al. (2021) for fractionations between intermediates and $\text{H}_2\text{O}_{(g)}$ or $\text{CO}_{2,(g)}$. Then, α^{eq} values against $\text{H}_2\text{O}_{(l)}$ were calculated from those against $\text{H}_2\text{O}_{(g)}$, using experimentally derived α values between $\text{H}_2\text{O}_{(l)}$ and $\text{H}_2\text{O}_{(g)}$ (Horita and Wesolowski, 1994).

3 Results

3.1 Batch culture experiment

The trends observed with increasing $\delta^{13}\text{C}_{\text{CH}_4}$ values and decreasing $\delta\text{D}_{\text{CH}_4}$ and $\Delta^{13}\text{CH}_3\text{D}$ values (Table 3) were consistent with those previously reported for a batch culture experiment with *M. bathoardescens* (Gruen et al., 2018). The carbon, hydrogen and clumped isotope fractionation factors ($^{13}\alpha$, $^2\alpha$ and γ , respectively) calculated following Gruen et al. (2018) were comparable to those reported previously: $^{13}\alpha$ of 0.98 (this study) compared to 0.97; $^2\alpha$ from 0.64 to 0.59 (this study) compared to 0.69 to 0.57; and γ of 1.0005 (this study) compared to 1.0020 and 1.0032 (Supplementary Material, Figure S1D, S1E and S1F).

3.2 Fed-batch culture experiments (*M. bathoardescens*)

The growth of *M. bathoardescens* in fed-batch experiments were characterized by linear increase in cell density (Supplementary Material, Figure S2A, S2D and S2G), consistent with previous observations with *M. bathoardescens* in fed-batch experiments (Ver Eecke et al., 2012). For all experiments, $^{13}\alpha$ decreased toward or went below that expected at $\text{CH}_4\text{-CO}_2$ equilibrium (Figure 3A4–3E4). $^2\alpha$ increased toward that expected at $\text{CH}_4\text{-H}_2\text{O}$ equilibrium; however, the final $^2\alpha$ values were still lower than that expected at equilibrium (Figure 3A5–3E5; Figure 4B). $\Delta^{13}\text{CH}_3\text{D}$ values

347 were low (range from -4.1 to 2.1%) compared to equilibrium, indicating strong kinetic
348 fractionations, and decreased over time (Figure 3A6–3E6; Figure 4C). Detailed observations for
349 each experiment are described below.

350 During Experiment F.82.80, *M. bathoardescens* was grown at $82\text{ }^{\circ}\text{C}$ and on 80% H_2 . $^{13}\alpha$
351 decreased from 0.957 to 0.944 (Figure 3A4; Figure 4A), and $^2\alpha$ increased from 0.674 to 0.708
352 (Figure 3A5; Figure 4B). $\Delta^{13}\text{CH}_3\text{D}$ values ranged from $1.25 \pm 0.48\%$ to $-0.29 \pm 0.47\%$ (Figure
353 3A6; Figure 4C). These $\Delta^{13}\text{CH}_3\text{D}$ values are lower than those expected at equilibrium (4.1% at
354 $82\text{ }^{\circ}\text{C}$). Notably, the changes in $\Delta^{13}\text{CH}_3\text{D}$ were in the direction away from the values expected at
355 equilibrium, unlike $^{13}\alpha$ and $^2\alpha$ values that changed toward equilibrium values.

356 During Experiment F.60.80, *M. bathoardescens* was grown at a suboptimal temperature of
357 $60\text{ }^{\circ}\text{C}$ and on 80% H_2 . $^{13}\alpha$ decreased from 0.982 to 0.964 (Figure 3B4; Figure 4A), and $^2\alpha$ increased
358 from 0.672 to 0.730 (Figure 3B5; Figure 4B). $\Delta^{13}\text{CH}_3\text{D}$ values ranged from $1.52 \pm 0.58\%$ to 0.06
359 $\pm 0.17\%$ (Figure 3B6; Figure 4C). These $\Delta^{13}\text{CH}_3\text{D}$ values are lower than those expected at
360 equilibrium (4.6% at $60\text{ }^{\circ}\text{C}$) and also in the direction away from the values expected at equilibrium.

361 During Experiment F.82.25, *M. bathoardescens* was grown at $82\text{ }^{\circ}\text{C}$ and on a lower x_{H_2} of 25%
362 H_2 . Comparable to the observations in F.82.80, $^{13}\alpha$ decreased from 0.963 to 0.941 during F.82.25
363 (Figure 3C4; Figure 4A), and $^2\alpha$ increased from 0.668 to 0.699 (Figure 3C5; Figure 4B). $\Delta^{13}\text{CH}_3\text{D}$
364 values ranged from $1.15 \pm 0.42\%$ to $-0.78 \pm 0.73\%$ (Figure 3C6; Figure 4C). The changes in
365 $\Delta^{13}\text{CH}_3\text{D}$ values during F.82.25 were also in the direction away from the values expected at
366 equilibrium, similar to the trends observed during F.82.80 and F.60.80.

367 The changes in bulk isotope values ($\delta^{13}\text{C}_{\text{CO}_2}$, $\delta^{13}\text{C}_{\text{CH}_4}$, $\delta\text{D}_{\text{H}_2\text{O}}$ and $\delta\text{D}_{\text{CH}_4}$) during F.82.80,
368 F.60.80 and F.82.25 are reported in Table 4 and Supplementary Material, Figure S3. Note that, for

369 F.82.25, the absolute $\delta^{13}\text{C}_{\text{CH}_4}$ values for F.82.25 are higher compared to those of F.82.80 because
370 different sources of CO_2 were used for the experiments.

371 3.3 Fed-batch culture experiments (*M. thermautotrophicus*)

372 The growth patterns of *M. thermautotrophicus* in fed-batch experiments were characterized by
373 distinct periods of exponential growth during the first 26 and 12 hours for F.65.20 (65 °C, 20% H_2)
374 and F.65.5 (65 °C, 5% H_2), respectively (Supplementary Material, Figure S4A and S4D). For
375 F.65.5, x_{H_2} in the supply gas was decreased from 5% to 1.6% after 55 hours. After decreasing the
376 x_{H_2} to 1.6%, the cell density remained relatively constant for the remainder of the experiment, and
377 x_{CH_4} and csMPR decreased (Supplementary Material, Figure S4F; Table 5).

378 $^{13}\alpha$ decreased from 0.966 to 0.950 during F.65.20 and from 0.957 to 0.938 during F.65.5
379 (Figure 3D4 and 3E4; Figure 4A). $^{2}\alpha$ slightly increased during F.65.20 and did not change
380 significantly during F.65.5 (Figure 3D5 and 3E5; Figure 4B). $\Delta^{13}\text{CH}_3\text{D}$ values decreased over time,
381 moving away from that expected at equilibrium, as was observed in *M. bathoardescens*
382 experiments (Figure 3D6 and 3E6; Figure 4B). Notably, the magnitudes of depletion (i.e., low
383 $\Delta^{13}\text{CH}_3\text{D}$ values) observed during F.65.20 and F.65.5 are comparable to those observed during
384 batch experiments with mesophilic methanogens, which tend to produce lower $\Delta^{13}\text{CH}_3\text{D}$ values
385 compared to thermophilic methanogens (open vs. filled circles; Figure 4C). The changes in bulk
386 isotope values ($\delta^{13}\text{C}_{\text{CO}_2}$, $\delta^{13}\text{C}_{\text{DIC}}$, $\delta^{13}\text{C}_{\text{CH}_4}$, $\delta\text{D}_{\text{H}_2\text{O}}$ and $\delta\text{D}_{\text{CH}_4}$) during F.65.20 and F.65.5 are reported
387 in Table 5 and Supplementary Material, Figure S5.

388 3.4 Dissolved H_2 in the liquid medium

389 The results of $[\text{H}_2]$ calculations are shown in Figure 3. Overall, the results show undersaturation
390 in $[\text{H}_2]$ with respect to headspace for high density and fast-growing cultures (Figure 3A1–4E1).

391 Media become more undersaturated over time (i.e., at higher cell density; Figure 3A2–3E2) due to
392 the increase in total H₂ consumption rate, which corresponds with the increase in *MPR* (Figure
393 3A3–3E3). The difference between the maximum [H₂]^{eq} and minimum [H₂] values (with lower
394 *k_La*) was the largest, between 2-fold and >10-fold, at the highest temperature (82 °C; F.82.80 and
395 F.82.25), whereas the difference was <2-fold at lower temperatures of 65°C and 60°C. The lower
396 range of [H₂] was calculated using the minimum *k_La* value required to avoid a negative [H₂] in all
397 experiments (350 h⁻¹), and the higher range of [H₂] was calculated with a *k_La* value of 350 h⁻¹,
398 twice as much as the minimum value (Figure 3A3–3E3).

399 3.5 Isotopologue flow network model

400 The equilibrium end-member scenario shows uniform values across the [H₂] range that correspond
401 to values expected at equilibrium (-51‰ for δ¹³C, -151‰ for δD and 6‰ for Δ¹³CH₃D at 82 °C,
402 yellow dotted line; Figure 5). The isotope values change as a function of [H₂] in the uniform
403 reversibility and differential reversibility scenarios (red dashed line and blue solid line,
404 respectively; Figure 5). The δ¹³C and Δ¹³CH₃D profiles show significant difference between
405 uniform and differential reversibility scenarios; in the differential reversibility scenario, δ¹³C and
406 Δ¹³CH₃D values decrease to local minima at a [H₂] range between the two *K_m* values assigned for
407 reversibility terms (i.e., 5×10⁻⁵ M for φ₁₋₃; 10⁻⁸ M for φ₄), and values increase toward the
408 equilibrium values when all four steps become reversible ([H₂] ≲ 10⁻⁷ M) (Figure 5A and 5C).
409 The low δ¹³C values between the two *K_m* values are less than the value expected for equilibrium.
410 In the Discussion section below, we provide further interpretations for the patterns of isotope
411 fractionation factors (¹³α, ²α) and clumped isotopologue abundance (Δ¹³CH₃D) observed during
412 fed-batch experiments in this study in light of [H₂] and isotopologue flow network model results.

413 4 Discussion

414 Our results—from combined analyses of $\delta^{13}\text{C}_{\text{CO}_2}$, $\delta^{13}\text{C}_{\text{CH}_4}$, $\delta\text{D}_{\text{H}_2\text{O}}$, $\delta\text{D}_{\text{CH}_4}$ and $\Delta^{13}\text{CH}_3\text{D}$ —confirm
415 previous observations that carbon isotope fractionation increases with decreasing $p\text{H}_2$ (Penning et
416 al., 2005; Londry et al., 2008; Okumura et al., 2016; Topçuoğlu et al., 2019; Nguyen et al., 2020)
417 and shed some new light on the behavior of hydrogen isotope and clumped isotopologue systems
418 at different growth phases and $[\text{H}_2]$. The observed values of consistently low $\delta\text{D}_{\text{CH}_4}$ and $\Delta^{13}\text{CH}_3\text{D}$
419 (relative to equilibrium) suggest primarily kinetic fractionations for hydrogen and clumped isotope
420 systems under our experimental conditions. However, the apparent decrease in $\Delta^{13}\text{CH}_3\text{D}$ values
421 (i.e., further departure from equilibrium) for later growth phase and low $[\text{H}_2]$ was unexpected and
422 contrasts previous model predictions based on the differential reversibility hypothesis (e.g., Stolper
423 et al., 2015; Wang et al., 2015). Using the modeled values of $[\text{H}_2]$ in the fed-batch system and
424 results of isotopologue flow network model, we discuss the observed patterns of $^{13}\alpha$ (section 4.1);
425 $^{2}\alpha$ and $\Delta^{13}\text{CH}_3\text{D}$ (section 4.2); limitations of the model and broader implications for interpreting
426 the isotopic signatures of natural methane samples (section 4.3).

427 4.1 High cell density during stationary growth phase leads to low $[\text{H}_2]$ and higher than
428 equilibrium carbon isotope fractionations

429 The magnitude of carbon isotope fractionation is higher (lower $^{13}\alpha$ values) for later growth phase
430 within a single experiment and at lower $x\text{H}_2$ across experiments (Figure 3A4–3E4; Figure 4A).
431 The decrease in $^{13}\alpha$ coincides with the transition from exponential phase to stationary phase for *M.*
432 *thermautotrophicus* (Figure 3D2 and 3E2) or later linear growth for *M. bathoardescens* (Figure
433 3A2–3C2). Our observation is consistent with previous culture studies that reported increasing
434 carbon isotope fractionation as a function of growth phase (Botz et al., 1996; Valentine et al., 2004)

435 and experiments with lower $p\text{H}_2$ (Valentine et al., 2004; Londry et al., 2008; Okumura et al., 2016;
436 Topçuoğlu et al., 2019; Nguyen et al., 2020). Some studies have also reported larger than
437 equilibrium isotope fractionation (e.g., Botz et al., 1996; Valentine et al., 2004; Penning et al.,
438 2005; Okumura et al., 2016; Topçuoğlu et al., 2019), similar to the observations in this study (e.g.,
439 F.82.80, F.82.25 and F.65.5 in Figure 3A4–3E4 and Figure 4A).

440 In addition to causing physiological changes, later growth phase with high cell density
441 leads to low $[\text{H}_2]$ due to the increase in total H_2 consumption rate. The decrease in $[\text{H}_2]$ at high cell
442 density is important to consider for the hydrogenotrophic methanogenesis reaction because of its
443 4:1 $\text{H}_2:\text{CH}_4$ stoichiometry (Eqn. 7) and poor solubility of H_2 . While the dissolved concentrations
444 of highly soluble gases (e.g., CO_2) can be close to equilibrium with the headspace, the dissolved
445 concentrations of poorly soluble gases (e.g., H_2 and CH_4) can be far away from equilibrium with
446 the gas phase. Higher partial pressure of water vapor at saturation ($p\text{H}_2\text{O}_{\text{sat}}$) in the reactor
447 headspace during (hyper)thermophilic incubations should also be considered (Eqn. 11), as it would
448 further lower the $[\text{H}_2]$ in liquid media. The observed linear growth for *M. bathoardescens* (Figure
449 3A2–3C2) suggests that growth and methane production rates were limited by the supply
450 (=dissolution) rate of H_2 .

451 Accurate measurement of $[\text{H}_2]$ for methanogenic media can be challenging. Previous
452 studies measured $[\text{H}_2]$ for fed-batch reactors or chemostats by sampling liquid media into serum
453 vials and measuring $p\text{H}_2$ in the headspace (e.g., Ver Eecke et al., 2012; Stewart et al., 2016;
454 Topçuoğlu et al., 2018, 2019). For example, Topçuoğlu et al. (2019) reported $[\text{H}_2]$ values (prior to
455 inoculation) of 82 ± 2 and 21 ± 6 μM for high and low H_2 experiments, respectively. These values
456 are lower and higher than the saturation concentrations (516 and 10 μM) based on the dry H_2
457 mixing ratios of 86.6 and 1.6% for high and low H_2 experiments, respectively. Here, high $p\text{H}_2\text{O}_{\text{sat}}$

458 at higher temperatures (0.51 bars at 82°C) can explain lower [H₂] compared to calculations for dry
459 headspace. Higher than saturation [H₂] values may indicate entrainment of H₂ microbubbles in
460 addition to dissolved H₂ (e.g., McGinnis et al., 2015). After inoculation, microbial consumption
461 of H₂ would affect the steady state dissolved concentrations of gases in the liquid due to relatively
462 slow rate of H₂ dissolution (Eqn. 12). For example, in anaerobic fermentors where H₂ is produced
463 by microbial processes, the liquid-to-gas mass transport limit resulted in as much as 80 times
464 oversaturation of H₂ compared to the headspace gas (Pauss et al., 1990). On the other hand, in
465 chemostat cultures where methanogens consume H₂ (i.e., gas-to-liquid transport), the dissolved H₂
466 concentration was found to be 10 times lower than the saturation with respect to gas phase (Jud et
467 al., 1997). Because methanogens use dissolved form of H₂, we estimated [H₂] under each
468 experimental condition to assess the effect of the dissolved H₂ concentration on isotope
469 fractionation.

470 As shown in Figure 6A, the modeled [H₂] range under our experimental conditions (*ca.* 7
471 to 410 μM) is lower than the [H₂] range expected for typical batch cultures (e.g., 0.6 to 1.2 mM
472 for 1 to 2 bars of 80% H₂ headspace) and partially overlaps with the [H₂] range found in cow rumen
473 (0.1 to 50 μM; Smolenski and Robinson, 1988; Janssen, 2010, and references therein; Wang et al.,
474 2015); but it is higher than the [H₂] range found in typical freshwater (5 to 75 nM; Robinson and
475 Tiedje, 1982; Conrad et al., 1985; Conrad et al., 1987; Kuivila et al., 1989) and marine sediments
476 (2 to 60 nM; Lin et al., 2012). In the differential reversibility scenario for the isotopologue flow
477 network model, δ¹³C values decrease with a decrease in [H₂] for [H₂] < 1 mM (between 10⁻⁶ and
478 10⁻³ M; Figure 5A). This is consistent with the decreasing ¹³α values observed during fed-batch
479 experiments with a decrease in [H₂] (due to increase in cell density) or xH₂ (mixing ratios for
480 different experiments) for the modeled [H₂] range between 7 and 410 μM (between 7×10⁻⁶ and

481 4×10^{-4} M; Figure 6B). In addition, the $^{13}\alpha$ values during the fed-batch experiment conducted at
482 82°C and 80% H_2 (F.82.80; $^{13}\alpha = 0.95 \pm 0.01$; Table 4, Figure 4A) were lower compared to the
483 $^{13}\alpha$ value for batch experiment conducted at the same temperature and initial $x\text{H}_2$ (B.82.80; $^{13}\alpha =$
484 0.98 ; Supporting Information, Figure S1D). Considering that $[\text{H}_2]$ in batch cultures at high
485 headspace pressure (1 to 2 bars) and $x\text{H}_2$ (80%) can reach millimolar levels (0.6 to 1.2 mM; Figure
486 6A), the difference in $^{13}\alpha$ values observed between fed-batch and batch experiments is also
487 consistent with the overall correlation between low $^{13}\alpha$ and low $[\text{H}_2]$.

488 Besides the general correlation between low $[\text{H}_2]$ and larger carbon isotope fractionation,
489 our isotopologue flow network model reproduced the large carbon isotope fractionation (larger
490 than equilibrium) observed during later growth phases in the differential reversibility scenario
491 (Figure 5A). When $[\text{H}_2]$ is between 5×10^{-5} and 10^{-8} M (i.e., two K_m values assigned for ϕ_1 to ϕ_3
492 and ϕ_4 , respectively), reactions up to $\text{CH}_3\text{-CoM}$ are largely reversible (ϕ_1 to $\phi_3 \simeq 1$). As a result,
493 $\delta^{13}\text{C}$ of the methyl group of $\text{CH}_3\text{-CoM}$ approaches to equilibrium value (-52‰ at 82°C ; Gropp et
494 al., 2021). The reversibility of the last step is relatively low above 10^{-8} M H_2 in our model, and
495 this step can result in kinetic isotope fractionation of up to -40‰ ($^{13}\alpha = 0.96 \pm 0.01$, assayed at
496 60°C ; Scheller et al., 2013). Accordingly, the maximum overall fractionation of $\sim -92\text{‰}$ ($-52 -$
497 40‰) can be achieved when the first three steps are fully reversible (ϕ_1 to $\phi_3 \simeq 1$) and the last step
498 is fully kinetic ($\phi_4 \simeq 0$). This is consistent with the minimum $^{13}\alpha$ value (0.908, or fractionation of
499 -92‰) in the differential reversibility scenario simulated at 60°C in our study (yellow solid line;
500 Figure 6B). At much lower $[\text{H}_2]$ (i.e., $< 10^{-8}$ M), the last step of methanogenesis becomes reversible
501 and equilibrium fractionation is expected (-57‰ at 60°C , -51‰ at 82°C ; Figure 6B).

502 4.2 Differential reversibility can explain the observed hydrogen and clumped isotopologue
503 systematics

504 Previous culture studies have so far exclusively produced non-equilibrium hydrogen isotope
505 fractionation (Valentine et al., 2004; Yoshioka et al., 2008; Hattori et al., 2012; Kawagucci et al.,
506 2014; Stolper et al., 2015; Okumura et al., 2016; Gruen et al., 2018). In this study, hydrogen isotope
507 system similarly indicated significant departure from equilibrium ($^2\alpha = 0.69 \pm 0.02$, Figure 3A5–
508 3E5, Figure 4B vs. $^2\alpha^{eq} = 0.81$ at 60 °C and 0.82 at 82 °C). In the differential reversibility scenario
509 (blue solid line; Figure 5B) δD values slightly increase for $[H_2] \geq 10^{-5}$ M, stay relatively constant
510 for the $[H_2]$ range between 10^{-5} M and 10^{-8} M, and significantly increase toward equilibrium value
511 for $[H_2] \leq 10^{-8}$ M (note that the two inflection points in the δD profile occur around the two K_m
512 values assigned for φ_1 to φ_3 and φ_4 , respectively). This is consistent with our isotope data for fed-
513 batch experiments for the modeled $[H_2]$ range between 7 and 410 μM (between 7×10^{-6} and $4 \times 10^{-}$
514 4 M), where relatively constant $^2\alpha$ values were observed (Figure 6B).

515 The relatively constant $^2\alpha$ for modeled $[H_2]$ between 10^{-5} M and 10^{-8} M in the differential
516 reversibility scenario (Figure 5B) and observed in our experiments (Figure 6C) can be explained
517 with a large KIE associated with the last step of methanogenesis (CH_3 -CoM to CH_4 reduction;
518 reaction 4, Figure 2A). As described above in section 4.1, reactions up to CH_3 -CoM are reversible
519 (φ_1 to $\varphi_3 \approx 1$) in the differential reversibility scenario for the $[H_2]$ range between 5×10^{-5} and 10^{-8}
520 M. Consequently, the three H atoms in the methyl group of CH_3 -CoM are isotopically equilibrated
521 with the surrounding water ($\delta D_{CH_3-CoM} = -122\text{‰}$ at 82 °C; Gropp et al., 2021). The reversibility
522 of the last step is relatively low at $[H_2] \geq 10^{-8}$ M in our model, and this step can result in large
523 kinetic isotope fractionation. For reference, Scheller et al., (2013) reported experimentally
524 determined values of primary KIE (k_H/k_D) of 2.44 (i.e., $^2,P\alpha$ of 0.41) and secondary KIE of 1.17

525 (i.e., $^{2,S}\alpha$ of 0.85) at 60 °C for the last step in reverse direction. The addition of the last H atom
526 from water (e.g., $\delta D_{H_2O} = -50\text{‰}$) to the equilibrated $CH_3\text{-CoM}$ with the $^{2,P}\alpha$ and $^{2,S}\alpha$ values above
527 would result in the final δD_{CH_4} of -343‰ ($= [\frac{3}{4} \cdot (-122/1000+1) \cdot (0.85) + \frac{1}{4} \cdot (-50/1000+1) \cdot$
528 $(0.41)] - 1$), which is comparable to the range observed in our experiments ($-339 \pm 34\text{‰}$; Table 4;
529 Table 5).

530 These experimental and model results together suggest that the persistent non-equilibrium
531 signatures observed for hydrogen isotope system in this study and previous studies are results of
532 differential reversibility with a less reversibility (larger KIE) at the last H-addition step. It follows
533 that, in our model setup, hydrogen isotope fractionation approaches to equilibrium values at sub-
534 μM ranges of $[H_2]$ (solid line, Figure 6C). Future experiments with direct measurements and
535 precise control of $[H_2]$ (e.g., continuous cultures) at sub- μM levels are needed to validate this
536 hypothesis.

537 Similar to $^{2,S}\alpha$ values, $\Delta^{13}CH_3D$ values were depleted and also indicated significant departure
538 from equilibrium; unlike in hydrogen isotope system, however, a distinct pattern of decreasing
539 $\Delta^{13}CH_3D$ values was observed for clumped isotope system (Figure 3A6–3E6; Figure 6D). This is
540 in sharp contrast with previous isotope model results that suggest a positive correlation between
541 the overall metabolic reversibility and $\Delta^{13}CH_3D$ (e.g., Stolper et al., 2015; Wang et al., 2015). In
542 this case, more reversibility would result in the increase of $\Delta^{13}CH_3D$ toward the value expected at
543 internal isotopologue equilibrium (*ca.* 4‰ at 82 °C). This unexpected pattern $\Delta^{13}CH_3D$ values was
544 reproduced in the differential reversibility scenario, with a distinct decrease in $\Delta^{13}CH_3D$ values for
545 the $[H_2]$ range between *ca.* 5×10^{-4} and 10^{-7} M (blue solid line, Figure 5C). Note that the two
546 inflection points in the $\Delta^{13}CH_3D$ profile occur around the two assigned K_m values of 5×10^{-5} and
547 10^{-8} M for ϕ_1 to ϕ_3 and ϕ_4 , respectively. The effect of assigned K_m values on the $\Delta^{13}CH_3D$ profile

548 was evident from sensitivity test results (Supplemental Material, Figure S6). The K_m value of
549 5×10^{-5} M for ϕ_1 to ϕ_3 resulted in the best fit to the $\Delta^{13}\text{CH}_3\text{D}$ values measured from the fed-batch
550 experiments in this study (e.g., panel C vs. panels A, B, D or E; Supplemental Material, Figure S6).
551 This is likely not a coincidence, given that the experimentally determined K_m value for
552 hyperthermophilic methanogens is close to the assigned value (6.6×10^{-5} M for three
553 *Methanocaldococcus* species; Ver Eecke *et al.*, 2012). Because our experiments were done at the
554 modeled $[\text{H}_2]$ range between 7 and 410 μM , we cannot empirically assess the fit of the lower K_m
555 value assigned for ϕ_4 in the differential reversibility scenario. For example, varying the $[\text{H}_2]$ value
556 for ϕ_4 between 10^{-10} and 10^{-6} M has negligible effect on the $\Delta^{13}\text{CH}_3\text{D}$ profile for $[\text{H}_2] \geq 10^{-6}$ M
557 (panels F–J; Supplemental Material, Figure S6). Future experiments at sub- μM levels of $[\text{H}_2]$ are
558 needed to properly determine the threshold K_m value for the last step of methanogenesis (which
559 may depend on the species) that would equilibrate $\Delta^{13}\text{CH}_3\text{D}$ signatures. However, the K_m value of
560 10^{-8} M for ϕ_4 used in this study is reasonable, considering that equilibrium $\Delta^{13}\text{CH}_3\text{D}$ signatures in
561 microbial methane have been found in marine sediments where the typical $[\text{H}_2]$ range is between
562 2 and 60 nM (Lin *et al.*, 2012; Figure 6A).

563 Another characteristic pattern of the clumped isotope system observed in our experiments
564 was significant depletion in $^{13}\text{CH}_3\text{D}$ with anti-clumped (negative) $\Delta^{13}\text{CH}_3\text{D}$ values at low $[\text{H}_2]$ or
565 $x\text{H}_2$ (Figure 3A6–3E6; Figure 6D). The differential reversibility scenario shown in Figure 5C and
566 Figure 6D successfully reproduces not only the decreasing trend but also anti-clumped $\Delta^{13}\text{CH}_3\text{D}$
567 values that fits the range of $\Delta^{13}\text{CH}_3\text{D}$ values observed in this study (minimum of -4.1%).
568 Sensitivity test results indicated that secondary clumped isotope fractionation of $\geq 6\%$ (i.e., $s_\gamma \geq$
569 0.994) is required to produce a distinct decreasing pattern with negative $\Delta^{13}\text{CH}_3\text{D}$ values at $[\text{H}_2] \geq$
570 10^{-5} M (i.e., lower end of our experimental range) (panels A–F; Supplemental Material, Figure

571 S7). The S_γ value of 0.990 (i.e., 10‰ secondary clumped isotope fractionation) resulted in the
572 profile that best fits both the decreasing trend and magnitude of depletion in measured $\Delta^{13}\text{CH}_3\text{D}$
573 values (Figure 5C, Figure 6D). Varying the magnitude of primary clumped isotope fractionation
574 (P_γ) without any secondary isotope fractionation ($S_\gamma=1$) did not reproduce the observed patterns in
575 $\Delta^{13}\text{CH}_3\text{D}$ (panels G–L; Supplemental Material, Figure S7).

576 4.3 Limitations of the isotopologue flow network model and implications for interpreting the 577 isotope signatures of natural methane samples

578 While we explored three different cases—including the differential reversibility scenario—for the
579 isotopologue flow network model, there is much complexity associated with the biochemical inner
580 workings of methanogenesis that is not captured in the model. The model uses a constant KIE
581 value per H-addition step, assuming that each step is catalyzed by the same enzyme across the
582 range of $[\text{H}_2]$ examined in this study (10^{-9} to 10^{-2} M). This may not be true for H-addition steps
583 that can be catalyzed by more than one enzyme (i.e., isoenzymes). There are at least two sets of
584 isoenzymes known to catalyze the second and fourth H-addition steps during hydrogenotrophic
585 methanogenesis. The fourth step of methanogenesis (the reduction of methenyl- H_4MPT^+ to
586 methylene- H_4MPT) involves either the oxidation of H_2 or the oxidation of the reduced form of F_{420}
587 (F_{420}H_2), where the former is catalyzed by H_2 -forming N^5,N^{10} -methylene- H_4MPT dehydrogenase
588 (Hmd) and the latter is catalyzed by F_{420} -dependent N^5,N^{10} -methylene- H_4MPT dehydrogenase
589 (Fmd) (von Büнау et al., 1991; Reeve et al., 1997). Previous studies have shown that Mtd increases
590 in expression, relative to Hmd, under H_2 limitation (Reeve et al., 1997; Hendrickson et al., 2007;
591 Topçuoğlu et al., 2019). The isoenzyme switching from Hmd to Mtd under H_2 limitation has been
592 suggested to allow a greater expression of carbon isotope fractionation (Valentine et al., 2004) and
593 may apply for hydrogen and clumped isotope systems as well.

594 Another set of isoenzymes, MCR I and MCR II (sometimes referred to as MR I and MR
595 II), catalyzes the fourth and last H-addition steps of hydrogenotrophic methanogenesis (Pihl et al.,
596 1994; Reeve et al., 1997). The relative abundances of MCR I and MCR II have been shown to be
597 determined largely by growth phase, where MCR II is preferentially expressed during exponential
598 phase and MCR I during linear or stationary phase (Rospert et al., 1990; Bonacker et al., 1992;
599 Pihl et al., 1994). Whether distinct KIEs are associated with these isoenzymes remains unclear;
600 however, considering that MCR I and MCR II have different substrate affinities (i.e., K_m values
601 for $\text{CH}_3\text{-S-CoM}$ and H-S-HTP) and catalytic rates (Bonacker et al., 1993), it is possible that these
602 isoenzymes for the rate-limiting step of last H-addition impart distinct KIEs. Future studies
603 combining a proteomic or transcriptomic approach and isotope analyses are needed to evaluate the
604 effect of isoenzyme switching on isotope fractionation during hydrogenotrophic methanogenesis.

605 Despite the limitations mentioned above, insights gained from the empirical relationships
606 among bulk ($^{13}\alpha$, $^2\alpha$) and clumped ($\Delta^{13}\text{CH}_3\text{D}$) isotope systems investigated in this study help us
607 better interpret the isotope signatures in natural samples of methane. Our experimental and model
608 results show that the nuances of isotope fractionation at a given time point warrant further
609 consideration of physiological state and the amount of H_2 available for methanogens in the
610 dissolved form. For example, rather than characterizing carbon isotope values with either an
611 equilibrium or kinetic end-member signature, one would need to consider the large carbon isotope
612 fractionation (larger than equilibrium) that can result from differential reversibility at an
613 intermediate range of $[\text{H}_2]$ (between 10^{-5} M and 10^{-8} M under our experimental conditions; Figure
614 5A).

615 Clumped isotope results also suggest that low $\Delta^{13}\text{CH}_3\text{D}$ values are not necessarily
616 associated with specific growth temperatures or metabolic pathways (e.g., hydrogenotrophic vs.

617 acetoclastic vs. methylotrophic). In studies where hydrogenotrophic species were grown on
618 H₂/CO₂ at different temperatures, mesophilic cultures in general were associated with larger
619 depletion in Δ¹³CH₃D compared to thermophilic cultures (Figure 4C; Stolper et al., 2015; Wang et
620 al., 2015; Gruen et al., 2018). In studies where methanogens were grown on different substrates
621 using different biochemical pathways, methylotrophic and acetoclastic cultures in general carried
622 more depleted Δ¹³CH₃D (and Δ¹²CH₂D₂) signatures (Young et al., 2017; Gruen et al., 2018). The
623 wide range of Δ¹³CH₃D values (−4.1 to 2.1‰) observed in this study, where all cultures were
624 grown under hyperthermophilic and hydrogenotrophic conditions, suggests that the magnitude of
625 depletion in clumped isotopologues is not always associated with growth temperatures or
626 methanogenic pathways.

627 **5 Conclusion**

628 We cultured two different species of methanogens, *Methanocaldococcus bathoardescens* and
629 *Methanothermobacter thermautotrophicus* (ΔH), in batch and fed-batch systems and measured the
630 δ¹³C and δD of the substrates (CO₂ and H₂O) as well as the δ¹³C, δD and Δ¹³CH₃D of the product
631 (CH₄). The results of the fed-batch experiments confirm previous observations, where carbon
632 isotope fractionation (¹³α = 0.96 ± 0.02) approaches and often exceed the magnitude expected at
633 CH₄-CO₂ equilibrium (e.g., Botz et al., 1996; Valentine et al., 2004; Penning et al., 2005; Okumura
634 et al., 2016; Topçuoğlu et al., 2019), while hydrogen isotope fractionation remains significantly
635 larger (²α = 0.67 ± 0.01) than that expected at CH₄-H₂O equilibrium (Figure 4). The observed low
636 Δ¹³CH₃D values indicate kinetic isotope effects, with an apparent decrease in Δ¹³CH₃D values with
637 decreasing p_{H₂}. The isotopologue flow network model presented showed our observations—large
638 carbon isotope fractionation, depleted hydrogen isotope signatures, and distinct decreasing
639 Δ¹³CH₃D values with decreasing p_{H₂}—can be explained by differential reversibility, in which the

640 last step of methanogenesis is less reversible compared to the preceding three H-addition reactions.
641 In addition, including secondary clumped KIE in the model reproduced the magnitude of depletion
642 in $\Delta^{13}\text{CH}_3\text{D}$ values observed in our experiments. Future studies focusing on controlled H_2
643 limitation experiments at sub- μM concentrations and conducting proteomic or transcriptomic
644 analyses in parallel may improve our interpretations of the bulk and clumped isotope signatures
645 used for methane source identification.

646

647 **Acknowledgment**

648 We thank J. F. Holden (University of Massachusetts, Amherst) for providing the *M.*
649 *bathoardescens* culture used in this study; T. Bosak for providing lab facilities to support our
650 culturing work; J. Sun for laboratory assistance for *M. thermautotrophicus* experiments; and D.
651 Boutt (University of Massachusetts, Amherst) for analyzing $\delta\text{D}_{\text{H}_2\text{O}}$. This work was supported by
652 the NASA Astrobiology Institute “Rock-Powered Life” project under cooperative agreement
653 NNA15BB02A. J.H.R. was also supported by the Grayce B. Kerr Fellowship, the Robert R. Shrock
654 Fellowship and the Callahan Dee Fellowship at MIT.

655

656 **Appendix A. Supplementary Material**

657 Research Data that supports this research publication can be found in the Supplementary Material
658 at [Link].

659

660 **References**

- 661 Balabane M., Galimov E., Hermann M. and Létolle R. (1987) Hydrogen and carbon isotope
662 fractionation during experimental production of bacterial methane. *Org. Geochem.* **11**, 115–
663 119.
- 664 Baldassare F. J., McCaffrey M. A. and Harper J. A. (2014) A geochemical context for stray gas
665 investigations in the northern Appalachian Basin: Implications of analyses of natural gases
666 from Neogene-through Devonian-age strata. *Am. Assoc. Pet. Geol. Bull.* **98**, 341–372.
- 667 Belyaev S. S., Wolkin R., Kenealy W. R., DeNiro M. J., Epstein S. and Zeikus J. G. (1983)
668 Methanogenic Bacteria from the Bondyuzhskoe Oil Field: General Characterization and
669 Analysis of Stable-Carbon Isotopic Fractionation. *Appl. Environ. Microbiol.* **45**, 691–697.
- 670 Bonacker L. G., Baudner S., Mörschel E., Böcher R. and Thauer R. K. (1993) Properties of the
671 two isoenzymes of methyl-coenzyme M reductase in *Methanobacterium*
672 *thermoautotrophicum*. *Eur. J. Biochem.* **217**, 587–595.
- 673 Bonacker L. G., Baudner S. and Thauer R. K. (1992) Erratum: Differential expression of the two
674 methyl-coenzyme M reductases in *Methanobacterium thermoautotrophicum* as described
675 immunochemically via isoenzyme-specific antisera (*European Journal of Biochemistry*,
676 Vol. 206, No. 1). *Eur. J. Biochem.* **207**, 1129.
- 677 Botz R., Pokojski H.-D., Schmitt M. and Thomm M. (1996) Carbon isotope fractionation during
678 bacterial methanogenesis reduction. **25**, 255–262.
- 679 von Büнау R., Zirngibl C., Thauer R. K. and Klein A. (1991) Hydrogen-forming and coenzyme-
680 F420-reducing methylene tetrahydromethanopterin dehydrogenase are genetically distinct
681 enzymes in *Methanobacterium thermoautotrophicum* (Marburg). *Eur. J. Biochem.* **202**,
682 1205–1208.

683 Cao X., Bao H. and Peng Y. (2019) A kinetic model for isotopologue signatures of methane
684 generated by biotic and abiotic CO₂ methanation. *Geochim. Cosmochim. Acta* **249**, 59–75.

685 Chabab S., Théveneau P., Coquelet C., Corvisier J. and Paricaud P. (2020) Measurements and
686 predictive models of high-pressure H₂ solubility in brine (H₂O+NaCl) for underground
687 hydrogen storage application. *Int. J. Hydrogen Energy* **45**, 32206–32220.

688 Conrad R., Goodwin S. and Zeikus J. G. (1987) Hydrogen metabolism in a mildly acidic lake
689 sediment (Knaack Lake). *FEMS Microbiol. Lett.* **45**, 243–249.

690 Conrad R., Phelps T. J. and Zeikus J. G. (1985) Gas metabolism evidence in support of the
691 juxtaposition of hydrogen-producing and methanogenic bacteria in sewage sludge and lake
692 sediments. *Appl. Environ. Microbiol.* **50**, 595–601.

693 Coplen T. B. (2011) Guidelines and recommended terms for expression of stable-isotope-ratio
694 and gas-ratio measurement results. *Rapid Commun. Mass Spectrom.* **25**, 2538–2560.

695 Douglas P. M. J., Stolper D. A., Eiler J. M., Sessions A. L., Lawson M., Shuai Y., Bishop A.,
696 Podlaha O. G., Ferreira A. A., Santos Neto E. V., Niemann M., Steen A. S., Huang L.,
697 Chimiak L., Valentine D. L., Fiebig J., Luhmann A. J., Seyfried W. E., Etiope G., Schoell
698 M., Inskeep W. P., Moran J. J. and Kitchen N. (2017) Methane clumped isotopes: Progress
699 and potential for a new isotopic tracer. *Org. Geochem.* **113**, 262–282. Available at:
700 <https://doi.org/10.1016/j.orggeochem.2017.07.016>.

701 Ver Eecke H. C., Butterfield D. A., Huber J. A., Lilley M. D., Olson E. J., Roe K. K., Evans L.
702 J., Merkel A. Y., Cantin H. V. and Holden J. F. (2012) Hydrogen-limited growth of
703 hyperthermophilic methanogens at deep-sea hydrothermal vents. *Proc. Natl. Acad. Sci. U.*
704 *S. A.* **109**, 13674–13679.

705 Etiope G. and Sherwood Lollar B. (2013) Abiotic methane on earth. *Rev. Geophys.* **51**, 276–299.

706 Flores R. M., Rice C. A., Stricker G. D., Warden A. and Ellis M. S. (2008) Methanogenic
707 pathways of coal-bed gas in the Powder River Basin, United States: The geologic factor.
708 *Int. J. Coal Geol.* **76**, 52–75.

709 Fuchs G., Moll J., Scherer P. and Thauer R. (1979a) Activity, acceptor specificity and function
710 of hydrogenase in *Methanobacterium thermoautotrophicum*. *Hydrog. Their Catal. Act.,*
711 *Struct. Funct., Work. Meet.*, 83–92.

712 Fuchs G., Thauer R., Ziegler H. and Stichler W. (1979b) Carbon Isotope Fractionation by
713 *Methanobacterium thermoautotrophicum*. **9**, 135–139.

714 Games L. M. and Hayes J. M. (1978) Methane-producing bacteria : natural frac ~ onatio ~ s of
715 the stable carbon isotopes. **42**, 1295–1297.

716 Gonzalez Y., Nelson D. D., Shorter J. H., McManus J. B., Dyroff C., Formolo M., Wang D. T.,
717 Western C. M. and Ono S. (2019) Precise Measurements of $^{12}\text{CH}_2\text{D}_2$ by Tunable Infrared
718 Laser Direct Absorption Spectroscopy. *Anal. Chem.* **91**, 14967–14974.

719 Gropp J., Iron M. A. and Halevy I. (2021) Theoretical estimates of equilibrium carbon and
720 hydrogen isotope effects in microbial methane production and anaerobic oxidation of
721 methane. *Geochim. Cosmochim. Acta* **295**, 237–264. Available at:
722 <https://doi.org/10.1016/j.gca.2020.10.018>.

723 Gruen D. S., Wang D. T., Ko M., Stewart L. C., Goldhammer T., Holden J. F., Hinrichs K. and
724 Ono S. (2018) ScienceDirect Experimental investigation on the controls of clumped
725 isotopologue and hydrogen isotope ratios in microbial methane. **237**, 339–356.

726 Hattori S., Nashimoto H., Kimura H., Koba K., Yamada K., Shimizu M., Watanabe H., Yoh M.
727 and Yoshida N. (2012) Hydrogen and carbon isotope fractionation by thermophilic
728 hydrogenotrophic methanogens from a deep aquifer under coculture with fermenters.

729 *Geochem. J.* **46**, 193–200.

730 Hayes J. M. (2001) Fractionation of carbon and hydrogen isotopes in biosynthetic processes.

731 *Rev. Mineral. Geochemistry* **43**, 225–277.

732 Haynes W. M., Lide D. R. and Bruno T. J. (2016) *CRC handbook of chemistry and physics: a*

733 *ready-reference book of chemical and physical data*. 97th Editi., CRC Press, Boca Raton,

734 Florida.

735 Hendrickson E. L., Haydock A. K., Moore B. C., Whitman W. B. and Leigh J. A. (2007)

736 Functionally distinct genes regulated by hydrogen limitation and growth rate in

737 methanogenic Archaea. **2007**.

738 Horibe Y. and Craig H. (1995) D/H fractionation in the system methane-hydrogen-water.

739 *Geochim. Cosmochim. Acta* **59**, 5209–5217.

740 Horita J. (2001) Carbon isotope exchange in the system CO₂-CH₄ at elevated temperatures.

741 *Geochim. Cosmochim. Acta* **65**, 1907–1919.

742 Horita J. and Wesolowski D. J. (1994) Horita and Wesolowski 1994. *Geochim. Cosmochim. Acta*

743 **58**, 1–13.

744 Janssen P. H. (2010) Influence of hydrogen on rumen methane formation and fermentation

745 balances through microbial growth kinetics and fermentation thermodynamics. *Anim. Feed*

746 *Sci. Technol.* **160**, 1–22.

747 Jud G., Schneider K. and Bachofen R. (1997) The role of hydrogen mass transfer for the growth

748 kinetics of *Methanobacterium thermoautotrophicum* in batch and chemostat cultures. *J. Ind.*

749 *Microbiol. Biotechnol.* **19**, 246–251.

750 Kawagucci S., Kobayashi M., Hattori S., Yamada K., Ueno Y., Takai K. and Yoshida N. (2014)

751 Hydrogen isotope systematics among H₂-H₂O-CH₄ during the growth of the

752 hydrogenotrophic methanogen *Methanothermobacter thermautotrophicus* strain Δ H.
753 *Geochim. Cosmochim. Acta* **142**, 601–614.

754 Krzycki J. A., Kenealy W. R., DeNiro M. J. and Zeikus J. G. (1987) Stable Carbon Isotope
755 Fractionation by *Methanosarcina barkeri* during Methanogenesis from Acetate, Methanol,
756 or Carbon Dioxide-Hydrogen. *Appl. Environ. Microbiol.* **53**, 2597–2599.

757 Kuivila K. M., Murray J. W., Devol A. H. and Novelli P. C. (1989) Methane production, sulfate
758 reduction and competition for substrates in the sediments of Lake Washington. *Geochim.*
759 *Cosmochim. Acta* **53**, 409–416.

760 Lin Y. S., Heuer V. B., Goldhammer T., Kellermann M. Y., Zabel M. and Hinrichs K. U. (2012)
761 Towards constraining H₂ concentration in subseafloor sediment: A proposal for combined
762 analysis by two distinct approaches. *Geochim. Cosmochim. Acta* **77**, 186–201.

763 Londry K. L., Dawson K. G., Grover H. D., Summons R. E. and Bradley A. S. (2008) Stable
764 carbon isotope fractionation between substrates and products of *Methanosarcina barkeri*.
765 *Org. Geochem.* **39**, 608–621.

766 Lovley D. R. (1985) Minimum threshold for hydrogen metabolism in methanogenic bacteria.
767 *Appl. Environ. Microbiol.* **49**, 1530–1531.

768 Macpherson J. V and Unwin P. R. (1997) Determination of the Diffusion Coefficient of
769 Hydrogen in Aqueous Solution Using Single and Double Potential Step
770 Chronoamperometry at a Disk Ultramicroelectrode. *Anal. Chem.* **69**, 2063–2069.

771 Mariotti A., Germon J. C., Hubert P., Kaiser P., Letolle R., Tardieux A. and Tardieux P. (1981)
772 Experimental determination of nitrogen kinetic isotope fractionation: Some principles;
773 illustration for the denitrification and nitrification processes. *Plant Soil* **62**, 413–430.

774 McGinnis D. F., Kirillin G., Tang K. W., Flury S., Bodmer P., Engelhardt C., Casper P. and

775 Grossart H. P. (2015) Enhancing surface methane fluxes from an oligotrophic lake:
776 Exploring the microbubble hypothesis. *Environ. Sci. Technol.* **49**, 873–880.

777 Nguyen T. B., Topçuoğlu B. D., Holden J. F., LaRowe D. E. and Lang S. Q. (2020) Lower
778 hydrogen flux leads to larger carbon isotopic fractionation of methane and biomarkers
779 during hydrogenotrophic methanogenesis. *Geochim. Cosmochim. Acta* **271**, 212–226.

780 Okumura T., Kawagucci S., Saito Y., Matsui Y., Takai K. and Imachi H. (2016) Hydrogen and
781 carbon isotope systematics in hydrogenotrophic methanogenesis under H₂-limited and H₂-
782 enriched conditions: implications for the origin of methane and its isotopic diagnosis. *Prog.*
783 *Earth Planet. Sci.* **3**, 1–19.

784 Ono S., Rhim J. H., Gruen D. S., Taubner H., Kölling M. and Wegener G. (2021) Clumped
785 isotopologue fractionation by microbial cultures performing the anaerobic oxidation of
786 methane. *Geochim. Cosmochim. Acta* **293**, 70–85.

787 Ono S., Wang D. T., Gruen D. S., Sherwood Lollar B., Zahniser M. S., McManus B. J. and
788 Nelson D. D. (2014) Measurement of a doubly substituted methane isotopologue, ¹³CH₃D,
789 by tunable infrared laser direct absorption spectroscopy. *Anal. Chem.* **86**, 6487–6494.

790 Park S. H., Park C., Lee J. Y. and Lee B. (2017) A Simple Parameterization for the Rising
791 Velocity of Bubbles in a Liquid Pool. *Nucl. Eng. Technol.* **49**, 692–699.

792 Pauss A., Andre G., Perrier M. and Guiot S. R. (1990) Liquid-to-Gas mass transfer in anaerobic
793 processes: Inevitable transfer limitations of methane and hydrogen in the biomethanation
794 process. *Appl. Environ. Microbiol.* **56**, 1636–1644.

795 Penning H., Plugge C. M., Galand P. E. and Conrad R. (2005) Variation of carbon isotope
796 fractionation in hydrogenotrophic methanogenic microbial cultures and environmental
797 samples at different energy status. *Glob. Chang. Biol.* **11**, 2103–2113.

798 Pihl T. D., Sharma S. and Reeve J. N. (1994) Growth phase-dependent transcription of the genes
799 that encode the two methyl coenzyme M reductase isoenzymes and N5-
800 methyltetrahydromethanopterin:Coenzyme M methyltransferase in *Methanobacterium*
801 *thermoautotrophicum* Δ H. *J. Bacteriol.* **176**, 6384–6391.

802 Pohlman J. W., Kaneko M., Heuer V. B., Coffin R. B. and Whiticar M. (2009) Methane sources
803 and production in the northern Cascadia margin gas hydrate system. *Earth Planet. Sci. Lett.*
804 **287**, 504–512.

805 Rees C. E. (1973) A steady-state model for sulphur isotope fractionation in bacterial reduction
806 processes. *Geochim. Cosmochim. Acta* **37**, 1141–1162.

807 Reeve J. N., Nölling J., Morgan R. M. and Smith D. R. (1997) Methanogenesis: Genes,
808 Genomes, and Who's on First? *J. Bacteriol.* **179**, 5975–5986.

809 Robinson J. A. and Tiedje J. M. (1982) Kinetics of hydrogen consumption by rumen fluid,
810 anaerobic digester sludge, and sediment. *Appl. Environ. Microbiol.* **44**, 1374–1384.

811 Rospert S., Linder D., Ellermann J. and Thauer R. K. (1990) Two genetically distinct methyl-
812 coenzyme M reductases in *Methanobacterium thermoautotrophicum* strain Marburg and
813 Δ H. *Eur. J. Biochem.* **194**, 871–877.

814 Scheller S., Goenrich M., Thauer R. K. and Jaun B. (2013) Methyl-Coenzyme M Reductase from
815 Methanogenic Archaea: Isotope Effects on the Formation and Anaerobic Oxidation of
816 Methane.

817 Schoell M. (1988) Multiple origins of methane in the Earth. *Chem. Geol.* **71**, 1–10.

818 Sherwood Lollar B., Lacrampe-Couloume G., Voglesonger K., Onstott T. C., Pratt L. M. and
819 Slater G. F. (2008) Isotopic signatures of CH₄ and higher hydrocarbon gases from
820 Precambrian Shield sites: A model for abiogenic polymerization of hydrocarbons. *Geochim.*

821 *Cosmochim. Acta* **72**, 4778–4795.

822 Sherwood Lollar B., Westgate T. D., Ward J. A., Slater G. F. and Lacrampe-Couloume G. (2002)

823 Abiogenic formation of alkanes in the earth's crust as a minor source for global

824 hydrocarbon reservoirs. *Nature* **416**, 522–524.

825 Smolenski W. J. and Robinson J. A. (1988) In situ rumen hydrogen concentrations in steers fed

826 eight times daily, measured using a mercury reduction detector. *FEMS Microbiol. Lett.* **53**,

827 95–100.

828 Stewart L. C., Llewellyn J. G., Butterfield D. A., Lilley M. D. and Holden J. F. (2016) Hydrogen

829 and thiosulfate limits for growth of a thermophilic, autotrophic *Desulfurobacterium* species

830 from a deep-sea hydrothermal vent. *Environ. Microbiol. Rep.* **8**, 196–200.

831 Stolper D. A., Martini A. M., Clog M., Douglas P. M., Shusta S. S., Valentine D. L., Sessions A.

832 L. and Eiler J. M. (2015) Distinguishing and understanding thermogenic and biogenic

833 sources of methane using multiply substituted isotopologues. *Geochim. Cosmochim. Acta*

834 **161**, 219–247.

835 Stolper D. A., Sessions A. L., Ferreira A. A., Santos Neto E. V., Schimmelmann A., Shusta S. S.,

836 Valentine D. L. and Eiler J. M. (2014) Combined ¹³C-D and D-D clumping in methane:

837 Methods and preliminary results. *Geochim. Cosmochim. Acta* **126**, 169–191. Available at:

838 <http://dx.doi.org/10.1016/j.gca.2013.10.045>.

839 Teramoto M., Fujita S., Kataoka M. and Hashimoto K. (1970) Effect of Bubble Size on the

840 Selectivity of Consecutive Gas-Liquid Reactions. In *Meeting of the Society of the Chemical*

841 *Engineers (Japan)* pp. 79–82.

842 Thauer R. K. (2011) Anaerobic oxidation of methane with sulfate: On the reversibility of the

843 reactions that are catalyzed by enzymes also involved in methanogenesis from CO₂. *Curr.*

844 *Opin. Microbiol.* **14**, 292–299.

845 Thauer R. K., Kaster A. K., Seedorf H., Buckel W. and Hedderich R. (2008) Methanogenic
846 archaea: Ecologically relevant differences in energy conservation. *Nat. Rev. Microbiol.* **6**,
847 579–591.

848 Topçuoğlu B. D., Meydan C., Orellana R. and Holden J. F. (2018) Formate hydrogenlyase and
849 formate secretion ameliorate H₂ inhibition in the hyperthermophilic archaeon
850 *Thermococcus paralvinellae*. *Environ. Microbiol.* **20**, 949–957.

851 Topçuoğlu B., Meydan C., Nguyen T., Lang S. and Holden J. F. (2019) Growth Kinetics, Carbon
852 Isotope Fractionation, and Gene Expression in the Hyperthermophile *Methanocaldococcus*
853 *jannaschii* during Hydrogen-Limited Growth and Interspecies Hydrogen Transfer Begüm.
854 **85**, 1–14.

855 Valentine D. L., Chidthaisong A., Rice A., Reeburgh W. S. and Tyler S. C. (2004) Carbon and
856 hydrogen isotope fractionation by moderately thermophilic methanogens. *Geochim.*
857 *Cosmochim. Acta* **68**, 1571–1590.

858 Wang D. T., Gruen D. S., Lollar B. S., Hinrichs K.-U., Stewart L. C., Holden J. F., Hristov A.
859 N., Pohlman J. W., Morrill P. L., Könneke M., Delwiche K. B., Reeves E. P., Sutcliffe C.
860 N., Ritter D. J., Seewald J. S., McIntosh J. C., Hemond H. F., Kubo M. D., Cardace D.,
861 Hoehler T. M. and Ono S. (2015) Nonequilibrium clumped isotope signals in microbial
862 methane. *Science (80-.)*. **348**, 428–431.

863 Welhan J. A. and Lupton J. E. (1987) Light hydrocarbon gases in Guaymas Basin hydrothermal
864 fluids: thermogenic versus abiogenic origin. *Am. Assoc. Pet. Geol. Bull.* **71**, 215–223.

865 Whiticar M. J. (1990) A geochemical perspective of natural gas and atmospheric methane. *Org.*
866 *Geochem.* **16**, 531–547.

867 Whiticar M. J. (1999) Carbon and hydrogen isotope systematics of bacterial formation and
868 oxidation of methane. *Chem. Geol.* **161**, 291–314.

869 Wolfe R. S. (2011) *Techniques for cultivating methanogens*. 1st ed., Elsevier Inc.

870 Yoshioka H., Sakata S. and Kamagata Y. (2008) Hydrogen isotope fractionation by
871 Methanothermobacter thermoautotrophicus in coculture and pure culture conditions.
872 *Geochim. Cosmochim. Acta* **72**, 2687–2694.

873 Young E. D., Kohl I. E., Lollar B. S., Etiope G., Rumble D., Li (李姝宁) S., Haghnegahdar M.
874 A., Schauble E. A., McCain K. A., Foustoukos D. I., Sutcliffe C., Warr O., Ballentine C. J.,
875 Onstott T. C., Hosgormez H., Neubeck A., Marques J. M., Pérez-Rodríguez I., Rowe A. R.,
876 LaRowe D. E., Magnabosco C., Yeung L. Y., Ash J. L. and Bryndzia L. T. (2017) The
877 relative abundances of resolved $^{12}\text{CH}_2\text{D}_2$ and $^{13}\text{CH}_3\text{D}$ and mechanisms controlling
878 isotopic bond ordering in abiotic and biotic methane gases. *Geochim. Cosmochim. Acta* **203**,
879 235–264.

880 Young E. D., Rumble D., Freedman P. and Mills M. (2016) A large-radius high-mass-resolution
881 multiple-collector isotope ratio mass spectrometer for analysis of rare isotopologues of O_2 ,
882 N_2 , CH_4 and other gases. *Int. J. Mass Spectrom.* **401**, 1–10.

883

884

885 **Tables**

886 Table 1. Summary of experiments.

Experiment	Organism	Temp. (°C)	xH ₂ (%)	System
B.82	<i>Methanocaldococcus bathoardescens</i>	82	80	Batch
F.82.80	<i>Methanocaldococcus bathoardescens</i>	82	80	Fed-batch
F.82.25	<i>Methanocaldococcus bathoardescens</i>	82	25	Fed-batch
F.60.80	<i>Methanocaldococcus bathoardescens</i>	60	80	Fed-batch
F65.20	<i>Methanothermobacter thermautotrophicus</i> (ΔH)	65	20	Fed-batch
F.65.5	<i>Methanothermobacter thermautotrophicus</i> (ΔH)	65	5→1.6	Fed-batch

887

888 Table 2. Parameters used for model calculation described in 2.3.7.

Parameter	Values used (range)	Sources/Notes
r _b	0.05 cm (0.025 to 0.1 cm)	Teramoto <i>et al.</i> (1970)
D	5 × 10 ⁻⁵ cm ² /sec	Macpherson and Unwin (1997)
A _b	200 cm ²	Calculated for a gas flow rate of 200 mL/min, medium height of 20 cm, and bubble radius of 0.05 cm; Park <i>et al.</i> (2017)
A _h	177 cm ²	Calculated for a known reactor I.D. = 15 cm

889

890 Table 3. Results for batch culture experiment (Experiment B.82). *Methanocaldococcus bathoardescens* was grown at
 891 82 °C on 80% H₂. The headspace pressure decreased, as 5 moles of gas were consumed to produce 1 mole of gas (Eqn.
 892 7). Therefore, volumes (in mL) of H₂, CO₂, and CH₄ were calculated assuming 4:1:1 reaction stoichiometries and
 893 mixing ratios for H₂: CO₂:CH₄ measure by GC (Table 3; Supplementary Material, Figure S1).

Time (h)	cells/mL	H ₂ (mL) [†]	CO ₂ (mL) [†]	CH ₄ (mL) [†]	δ ¹³ C _{CO2} (‰)	δ ¹³ C _{CH4} (‰)	δD _{H2O} (‰)	δD _{CH4} (‰)	Δ ¹³ CH ₃ D (‰)	CI
0.0	-	288.24	47.35	0.13	-34.9	-	-45.4	-	-	-
1.0	1.1E+6	281.61	50.49	0.53	-	-	-46.9	-	-	-
1.9	5.5E+6	258.65	44.57	6.83	-31.4	-	-	-	-	-
3.0	3.7E+7	125.88	13.33	36.98	-14.3	-47.1	-46.5	-407.6	0.48	0.20
4.0	3.6E+7	78.29	4.55	48.45	-25.1	-39.5	-	-409.6	0.38	0.19
5.0	7.4E+7	68.78	2.84	50.48	-	-	-	-	-	-
6.0	7.1E+7	35.52	2.60	58.35	-22.0	-	-	-	-	-
6.9	4.3E+7	53.28	2.11	53.90	-	-38.8	-46.0	-413.3	0.32	0.26

894

895 [†] volume of gas calculated based on mixing ratios and expected headspace pressure at the time of measurement; –
 896 values not determined; CI is the 95% confidence interval in permil (‰).

897 Table 4. Results for fed-batch experiments. *Methanocaldococcus bathoardescens* was grown at 82 °C and 80% H₂ (F.82.80); at 60 °C and 80% H₂ (F.60.80); and
 898 at 82 °C and 25% H₂ (F.82.25).

Experiment	Temp (°C)	Time (h)	cells/mL	H ₂ (%)	CO ₂ (%)	CH ₄ (%)	MPR (mol/h)	csMPR (pmol/cell/h)	δ ¹³ C _{CO2} (‰)	δ ¹³ C _{CH4} (‰)	α _{CH4 CO2}	δD _{H2O} (‰)	δD _{CH4} (‰)	α _{CH4 H2O}	Δ ¹³ CH ₃ D (‰)	CI
F.82.80	82	0.0	6.8E+5	79.8	19.9	0.08	4.1E-04	0.33	-39.9	-	*	-53.7	-	*	-	-
F.82.80	82	0.0	-	80.7	19.5	1.78	8.0E-03	-	-	-	*	-	-	*	-	-
F.82.80	82	1.1	5.2E+6	-	-	-	-	-	-	-	*	-	-	*	-	-
F.82.80	82	1.5	-	76.6	20.0	3.75	1.6E-02	-	-25.8	-68.2	0.957	-53.8	-362.6	0.674	1.25	0.48
F.82.80	82	2.2	2.0E+7	77.2	19.8	4.03	1.7E-02	0.47	-21.3	-76.6	0.944	-	-336.9	*	0.38	0.43
F.82.80	82	2.5	2.8E+7	77.9	18.5	4.02	1.7E-02	0.34	-	-74.3	*	-	-331.8	*	-0.17	0.49
F.82.80	82	3.0	3.2E+7	78.0	18.6	4.09	1.7E-02	0.29	-	-80.2	*	-	-333.6	*	0.07	0.83
F.82.80	82	3.5	4.1E+7	-	-	-	-	-	-	-	*	-	-	*	-	-
F.82.80	82	3.7	4.5E+7	77.0	19.2	3.92	1.7E-02	0.21	-	-77.9	*	-	-331.8	*	-0.29	0.47
F.60.80	60	0.0	5.8E+6	75.5	21.9	0.06	3.1E-04	0.03	-	-	*	-	-	*	-	-
F.60.80	60	1.5	1.7E+7	73.9	22.3	0.47	2.4E-03	0.08	-38.8	-56.4	0.982	-	-305.0	*	2.06	-
F.60.80	60	1.8	-	75.3	22.1	0.50	2.6E-03	-	-	-	*	-	-	*	-	-
F.60.80	60	2.8	1.4E+7	73.1	22.4	1.38	6.9E-03	0.28	-	-	*	-	-	*	-	-
F.60.80	60	3.3	-	75.1	22.2	1.90	9.0E-03	-	-36.8	-60.1	0.976	-	-364.5	*	1.52	0.58
F.60.80	60	3.8	2.4E+7	72.5	21.1	2.98	1.4E-02	0.32	-	-	*	-	-	*	-	-
F.60.80	60	5.6	1.3E+8	74.0	21.1	4.14	1.8E-02	0.08	-	-	*	-	-	*	-	-
F.60.80	60	6.4	-	74.5	21.0	3.94	1.7E-02	-	-33.6	-68.9	0.964	-	-321.4	*	0.80	0.28
F.60.80	60	6.7	1.1E+8	71.7	21.3	3.64	1.7E-02	0.08	-	-	*	-	-	*	-	-
F.60.80	60	7.8	1.4E+8	73.9	21.4	3.91	1.7E-02	0.07	-	-	*	-	-	*	-	-
F.60.80	60	8.9	1.9E+8	71.7	21.2	3.7	1.7E-02	0.05	-	-	*	-	-	*	-	-
F.60.80	60	9.4	-	73.7	21.6	4.07	1.8E-02	-	-32.6	-67.5	0.964	-	-314.6	*	0.06	0.17
F.82.25	82	0.0	1.0E+6	23.1	21.8	BDL	-	-	-	-	*	-	-	*	-	-
F.82.25	82	0.2	-	23.1	21.9	0.03	1.6E-04	-	-14.0	-50.8	0.963	-40.4	-358.8	0.668	1.15	0.42
F.82.25	82	0.5	4.4E+6	22.8	23.6	0.41	2.1E-03	0.27	-	-	*	-	-	*	-	-
F.82.25	82	1.7	1.3E+7	22.6	22.9	1.30	5.8E-03	0.25	-	-	*	-39.9	-	*	-	-
F.82.25	82	2.3	9.1E+6	22.5	23.8	1.39	6.1E-03	0.37	-	-	*	-	-	*	-	-
F.82.25	82	2.8	9.6E+6	22.4	23.5	1.53	6.6E-03	0.38	-	-	*	-40.1	-	*	-	-
F.82.25	82	3.6	2.1E+7	22.4	23.8	1.56	6.7E-03	0.18	-	-	*	-	-	*	-	-
F.82.25	82	4.4	7.4E+6	22.5	23.9	1.47	6.4E-03	0.48	-	-	*	-40.0	-	*	-	-
F.82.25	82	4.9	2.4E+7	22.4	24.2	1.57	6.7E-03	0.16	-	-	*	-	-	*	-	-
F.82.25	82	5.2	2.8E+7	16.7	22.8	1.41	7.8E-03	0.15	-	-	*	-	-	*	-	-
F.82.25	82	19.0	2.0E+8	22.6	23.6	1.69	7.1E-03	0.02	-	-	*	-	-	*	-	-
F.82.25	82	22.5	1.0E+8	22.6	23.9	1.51	6.5E-03	0.04	-	-	*	-	-	*	-	-
F.82.25	82	24.5	9.6E+7	22.6	23.3	1.57	6.7E-03	0.04	-	-	*	-	-	*	-	-
F.82.25	82	24.7	-	22.4	23.9	1.82	7.5E-03	-	-12.0	-70.8	0.941	-	-328.6	*	-0.78	0.73
F.82.25	82	25.8	8.1E+7	22.5	23.0	1.65	7.0E-03	0.05	-	-	*	-	-	*	-	-
F.82.25	82	26.8	1.0E+8	22.2	2.0	2.05	8.3E-03	0.05	-	-	*	-	-	*	-	-
F.82.25	82	43.7	1.5E+8	21.6	23.8	2.82	1.1E-02	0.04	-	-	*	-	-	*	-	-
F.82.25	82	44.4	-	21.6	24.8	2.71	1.0E-02	-	-9.9	-67.8	0.941	-	-327.7	*	-0.65	0.36
F.82.25	82	45.2	-	21.7	23.3	2.89	1.1E-02	-	-10.3	-65.4	0.944	-38.6	-364.5	0.661	-0.42	0.53
F.82.25	82	52.5	2.1E+8	21.2	24.9	2.62	1.0E-02	0.03	-	-	*	-	-	*	-	-

899
 900 – values not determined; * not applicable; CI is the 95% confidence interval in permil (‰).

901 Table 5. Results for fed-batch experiments. *Methanothermobacter thermautotrophicus* was grown at 65 °C and 20% H₂ (Experiment F.65.20) and at 65 °C and 5–
 902 1.6% H₂ (Experiment F.65.5).

Experiment	Time (h)	cells/mL	H ₂ (%)	CO ₂ (%)	CH ₄ (%)	MPR (mol/h)	csMPR (pmol/cell/h)	δ ¹³ C _{CO2} (‰)	δ ¹³ C _{DIC} (‰)	α _{CO2-DIC}	δ ¹³ C _{CH4} (‰)	α _{CH4-CO2}	δD _{H2O} (‰)	δD _{CH4} (‰)	α _{CH4-H2O}	Δ ¹³ CH ₃ D (‰)	CI
F.65.20	0.0	2.3E+5	21.6	18.7	0.01	4.1E-05	0.098	-15.3	-11.7	0.996	-	*	-45.5	-	*	-	-
F.65.20	2.2	4.8E+5	21.2	19.4	0.03	1.4E-04	0.158	-	-	*	-	*	-	-	*	-	-
F.65.20	5.8	1.2E+6	21.1	19.3	0.10	4.5E-04	0.213	-	-	*	-	*	-	-	*	-	-
F.65.20	11.7	4.8E+6	19.9	19.3	0.44	2.0E-03	0.237	-14.9	-10.5	0.996	-48.4	0.966	-45.5	-361.8	0.669	0.33	0.57
F.65.20	22.8	4.8E+7	19.5	17.9	0.69	3.0E-03	0.035	-14.9	-9.7	0.995	-57.0	0.957	-	-363.3	0.667	-2.03	0.50
F.65.20	25.7	6.9E+7	19.5	18.1	0.70	3.1E-03	0.025	-	-	*	-	*	-	-	*	-	-
F.65.20	28.1	7.7E+7	19.5	18.1	0.70	3.1E-03	0.022	-	-9.7	*	-	*	-45.5	-	*	-	-
F.65.20	33.3	1.1E+8	19.5	18.1	0.71	3.1E-03	0.016	-14.0	-	*	-	*	-	-	*	-	-
F.65.20	47.2	1.8E+8	19.3	18.7	0.72	3.2E-03	0.010	-13.9	-9.4	0.995	-62.1	0.951	-	-347.0	0.684	-1.28	0.87
F.65.20	53.2	2.1E+8	19.2	19.3	0.74	3.3E-03	0.009	-13.6	-9.5	0.996	-	*	-	-	*	-	-
F.65.20	70.2	2.9E+8	19.3	18.1	0.76	3.3E-03	0.007	-	-	*	-	*	-	-	*	-	-
F.65.20	77.0	2.7E+8	19.3	19.0	0.76	3.3E-03	0.007	-13.6	-9.4	0.996	-62.9	0.950	-	-352.3	0.679	-1.09	0.65
F.65.20	94.9	3.1E+8	19.4	18.8	0.78	3.4E-03	0.006	-	-	*	-	*	-	-	*	-	-
F.65.20	101.9	4.5E+8	19.0	18.9	0.81	3.6E-03	0.004	-13.8	-9.6	0.996	-63.3	0.950	-	-351.4	0.677	-1.91	0.54
F.65.20	102.4	3.9E+8	19.2	19.5	0.80	3.5E-03	0.005	-	-	*	-	*	-	-	*	-	-
F.65.20	119.2	4.1E+8	18.9	19.5	0.80	3.5E-03	0.005	-	-	*	-	*	-41.4	-	*	-	-
F.65.5	0.0	2.8E+5	4.9	20.3	0.01	5.2E-05	0.103	-15.7	-11.4	0.996	-	-	-44.9	-	*	-	-
F.65.5	1.7	4.7E+5	4.8	19.6	0.04	1.8E-04	0.210	-	-	*	-	-	-	-	*	-	-
F.65.5	4.9	1.1E+6	4.5	20.7	0.09	4.7E-04	0.252	-	-	*	-	-	-	-	*	-	-
F.65.5	9.4	2.5E+6	4.4	19.7	0.1	7.0E-04	0.156	-	-	*	-58.0	0.957	-	-364.1	0.666	1.28	0.98
F.65.5	10.5	-	-	-	-	-	-	-15.5	-11.4	0.996	-	-	-	-	*	-	-
F.65.5	11.8	5.9E+6	4.4	19.6	0.14	7.1E-04	0.068	-	-	*	-	-	-	-	*	-	-
F.65.5	21.9	1.4E+7	4.3	20.5	0.16	7.9E-04	0.031	-	-	*	-67.0	0.947	-	-371.7	0.658	-2.06	0.47
F.65.5	23.3	-	-	-	-	-	-	-15.2	-10.9	0.996	-	-	-45.5	-	*	-	-
F.65.5	27.5	2.5E+7	4.4	19.3	0.16	7.7E-04	0.017	-	-	*	-	-	-	-	*	-	-
F.65.5	30.3	2.7E+7	4.4	19.0	0.16	7.7E-04	0.016	-	-11.0	*	-	-	-	-	*	-	-
F.65.5	46.0	5.1E+7	4.3	20.6	0.17	8.2E-04	0.009	-	-	*	-	-	-	-	*	-	-
F.65.5	54.0	5.8E+7	4.3	19.5	0.17	8.5E-04	0.008	-15.3	-11.3	0.996	-70.6	0.944	-45.2	-368.4	0.661	-2.92	0.84
F.65.5	72.5	6.6E+7	1.6	20.3	0.06	2.5E-04	0.002	-15.6	-11.5	0.996	-77.5	0.937	-	-365.3	0.665	-2.52	0.46
F.65.5	95.3	7.2E+7	1.6	20.1	0.06	2.5E-04	0.002	-	-	*	-76.9	0.938	-	-370.0	0.660	-4.13	0.46
F.65.5	97.3	-	-	-	-	-	-	-15.6	-11.4	0.996	-	-	-	-	*	-	-
F.65.5	119.4	7.0E+7	1.5	21.4	0.06	2.6E-04	0.002	-	-	*	-	-	-	-	*	-	-

903

904 – values not determined; * not applicable; CI is the 95% confidence interval in permil (‰)

905 **Figure Captions**

906 **Figure 1.** Schematic diagram of the fed-batch culturing system

907 **Figure 2.** Schematic overview of the biochemical pathway involved in hydrogenotrophic
908 methanogenesis and isotopologue flow network model scenarios in this study. (A) Overview of
909 the biochemical pathway and enzymes associated with each step. Grey bubbles represent pools of
910 cellular carbon, grouped into those with the same redox state. The four H-addition steps are labeled
911 with numbers. Fd_{red} , reduced ferredoxin; Fd_{ox} , oxidized ferredoxin; MFR, methanofuran; H_4MPT ,
912 tetrahydromethanopterin; F_{420} , coenzyme F_{420} ; CoM-HS, coenzyme M; CoB-SH, coenzyme B; Ftr,
913 formyl-MFR: H_4MPT formyltransferase; Mch, N^5, N^{10} -methenyl- H_4MPT cyclohydrolase; Mtd,
914 F_{420} -dependent N^5, N^{10} -methylene- H_4MPT dehydrogenase; Hmd, H_2 -forming N^5, N^{10} -methylene-
915 H_4MPT dehydrogenase; Mer, F_{420} -dependent N^5, N^{10} -methylene- H_4MPT reductase; Mtr, N^5 -
916 methyl- H_4MPT :CoM methyltransferase; Mcr, methyl CoM reductase. Panels B, C and D show
917 the three model scenarios tested in this study. K_m values are effective half-saturation constants
918 used to assign reversibilities to H-addition steps. (B) Equilibrium end-member scenario has a K_m
919 value of 10^4 M for all four H-addition steps. (C) Uniform reversibility scenario has a K_m value of
920 10^{-8} M for all four H-addition steps. (D) In differential reversibility scenario, the last step is less
921 reversible compared to the preceding three H-addition steps ($K_m = 5 \times 10^{-5}$ M for the first three
922 steps; $K_m = 10^{-8}$ M for the last step).

923 **Figure 3.** Summary of fed-batch experiment results of this study. Each column (columns A–E)
924 shows the result for each fed-batch experiment. The experiment names and conditions can be found
925 at the top of each column. Each row (rows 1–6) shows a type of data. Modeled values of dissolved
926 hydrogen concentration or $[H_2]$ (μM ; row 1), cell density (cells/mL; row 2), methane production
927 rate or MPR ($\mu mol/sec$; row 3), carbon isotope fractionation factor or $^{13}\alpha$ (row 4), hydrogen isotope

928 fractionation factor or $^2\alpha$ (row 5), and methane clumped isotope abundance or $\Delta^{13}\text{CH}_3\text{D}$ (‰; row
929 6). For the $[\text{H}_2]$ model results (row 1), open squares represent maximum $[\text{H}_2]$ values expected at
930 equilibrium with the dry headspace mixing ratios ($x\text{H}_2$). Filled circles represent $[\text{H}_2]$ values
931 expected at equilibrium that are corrected for saturation water vapor pressure ($p\text{H}_2\text{O}_{\text{sat}}$) at
932 respective temperatures (0.51 bars at 82 °C, 0.25 bars at 65 °C and 0.20 bars at 60 °C). Triangles
933 represent $p\text{H}_2\text{O}_{\text{sat}}$ -corrected $[\text{H}_2]$ values expected during methane production with two different
934 k_La values: 700 h^{-1} (down-pointing yellow triangles) and 350 h^{-1} (up-pointing blue triangles).
935 Refer to 2.3.7 for details. Grey horizontal lines in rows 4–6 represent the equilibrium $^{13}\alpha$, $^2\alpha$ and
936 $\Delta^{13}\text{CH}_3\text{D}$ values expected at respective experimental temperatures. Grey vertical lines in column
937 5 for F.65.5 indicate the time at which $x\text{H}_2$ was switched from 5% to 1.6%. Each panel shares the
938 y-axis with the panel to its left unless new axis tick marks are introduced. Note that the durations
939 of experiments vary across experiments.

940 **Figure 4.** Changes in carbon ($^{13}\alpha$) and hydrogen ($^2\alpha$) isotope fractionation factors and $\Delta^{13}\text{CH}_3\text{D}$
941 values during hydrogenotrophic methanogenesis. Panels A, B and C, respectively, show $^{13}\alpha$, $^2\alpha$
942 and $\Delta^{13}\text{CH}_3\text{D}$ values measured in this study and reported in the literature, as a function of H_2 partial
943 pressure ($p\text{H}_2$) in the supply gas. Color triangle and diamond symbols represent data from this
944 study. Grey circles in panels A and B represent the $^{13}\alpha$ and $^2\alpha$ values from the literature (Games
945 and Hayes, 1978; Fuchs *et al.*, 1979; Belyaev *et al.*, 1983; Balabane *et al.*, 1987; Krzycki *et al.*,
946 1987; Botz *et al.*, 1996; Valentine *et al.*, 2004; Yoshioka, Sakata and Kamagata, 2008; Hattori *et*
947 *al.*, 2012; Kawagucci *et al.*, 2014). Grey symbols in panel C represent the $\Delta^{13}\text{CH}_3\text{D}$ values obtained
948 from pure culture hydrogenotrophic methanogenesis experiments in closed systems (Gruen *et al.*,
949 2018 and references therein). Filled and open circles represent thermophilic and mesophilic
950 temperatures, respectively. Dashed lines represent the $^{13}\alpha$, $^2\alpha$ and $\Delta^{13}\text{CH}_3\text{D}$ values expected at

951 equilibrium at temperatures indicated in the legend.

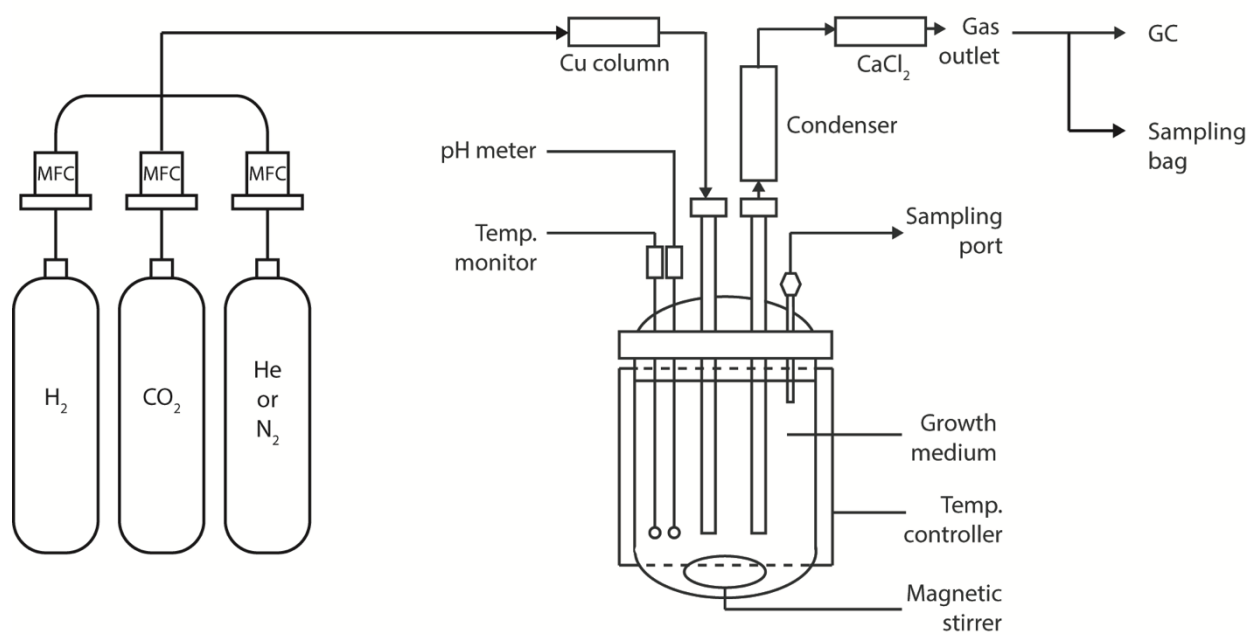
952 **Figure 5.** Modeled carbon ($\delta^{13}\text{C}$) and hydrogen (δD) isotope and clumped isotopologue
953 compositions ($\Delta^{13}\text{CH}_3\text{D}$) of methane produced via hydrogenotrophic methanogenesis. Panel A, B,
954 and C show the modeled $\delta^{13}\text{C}$, δD and $\Delta^{13}\text{CH}_3\text{D}$ values of methane, respectively. Dotted lines
955 (yellow) show the model results at 82 °C for the equilibrium end-member scenario ($K_m = 10^4$ M
956 for all ϕ values). Dashed lines (red) show the results for the uniform reversibility scenario ($K_m =$
957 10^{-8} M for all ϕ values). Solid lines (blue) show a differential reversibility scenario, where the last
958 H-addition step is less reversible compared to the preceding three H-addition steps ($K_m = 5 \times 10^{-5}$
959 M for ϕ_{1-3} , $K_m = 10^{-8}$ M for ϕ_4).

960 **Figure 6.** Carbon ($^{13}\alpha$) and hydrogen ($^2\alpha$) isotope fractionation factors and $\Delta^{13}\text{CH}_3\text{D}$ values as a
961 function of modeled dissolved H_2 concentration, $[\text{H}_2]$. Panel A shows the typical ranges of $[\text{H}_2]$
962 observed in natural environments and culture studies. The $[\text{H}_2]$ ranges for batch cultures studies
963 were calculated assuming 1–2 bars of 80% H_2 in the headspace at 25 °C. Note that the $p\text{H}_2$ values
964 for batch co-cultures (Okumura et al., 2016) are based on headspace mixing ratios and that $[\text{H}_2]$ in
965 the co-cultures are likely higher than $[\text{H}_2]^{\text{eq}}$ expected in equilibrium with $p\text{H}_2$. Panels B, C and D
966 compare the result of the isotopologue flow network model and experimental data from this study.
967 Color symbols and corresponding experiment names are shown in the legend. Horizontal dashed
968 lines represent the $^{13}\alpha$, $^2\alpha$ and $\Delta^{13}\text{CH}_3\text{D}$ values expected at equilibrium at corresponding
969 temperatures as shown in the legend. Solid lines are modeled trajectories of $^{13}\alpha$, $^2\alpha$ and $\Delta^{13}\text{CH}_3\text{D}$
970 for the differential reversibility scenario based on the isotopologue flow network model results
971 (see Figure 5).

972

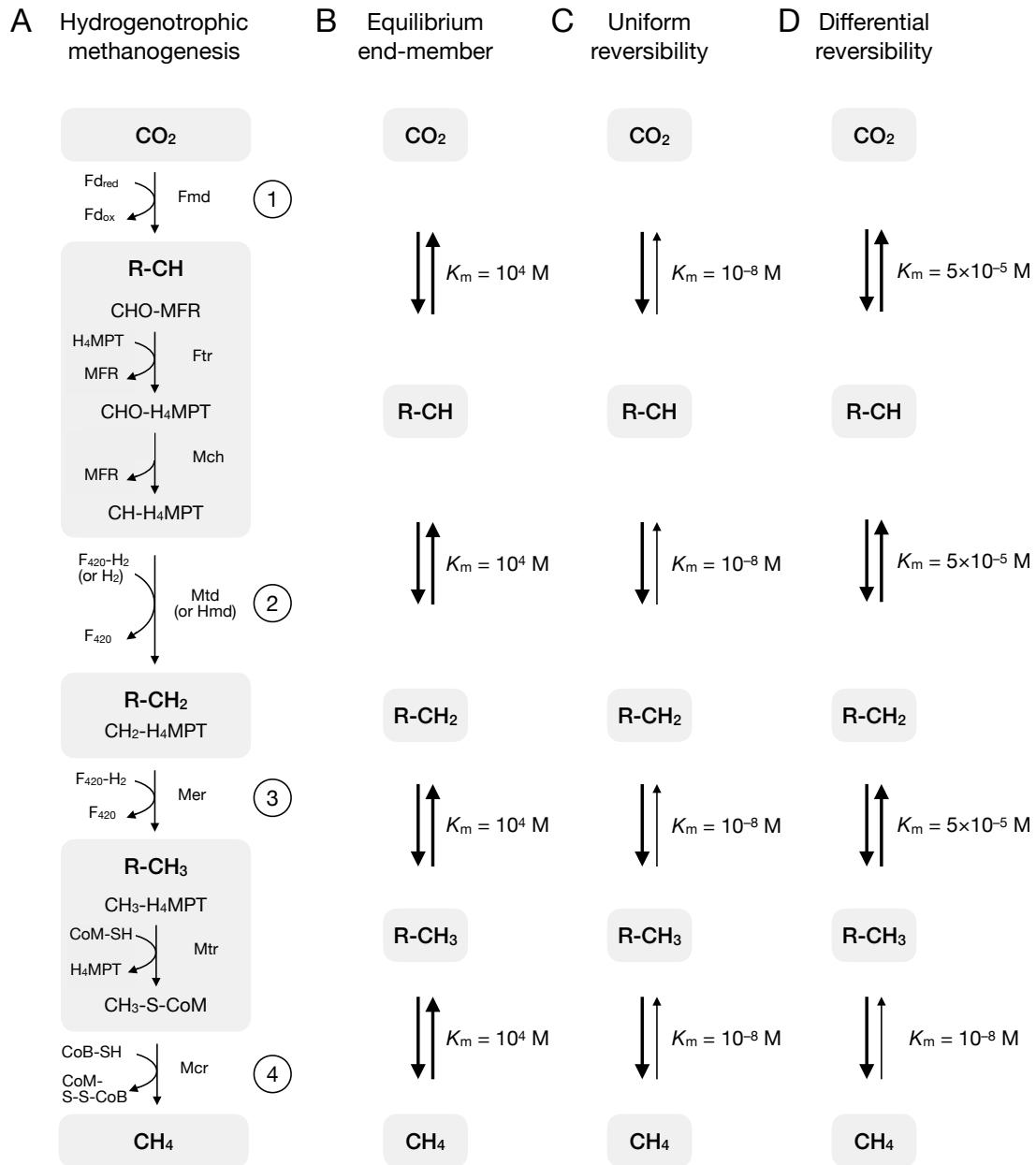
973 **Figures**

974

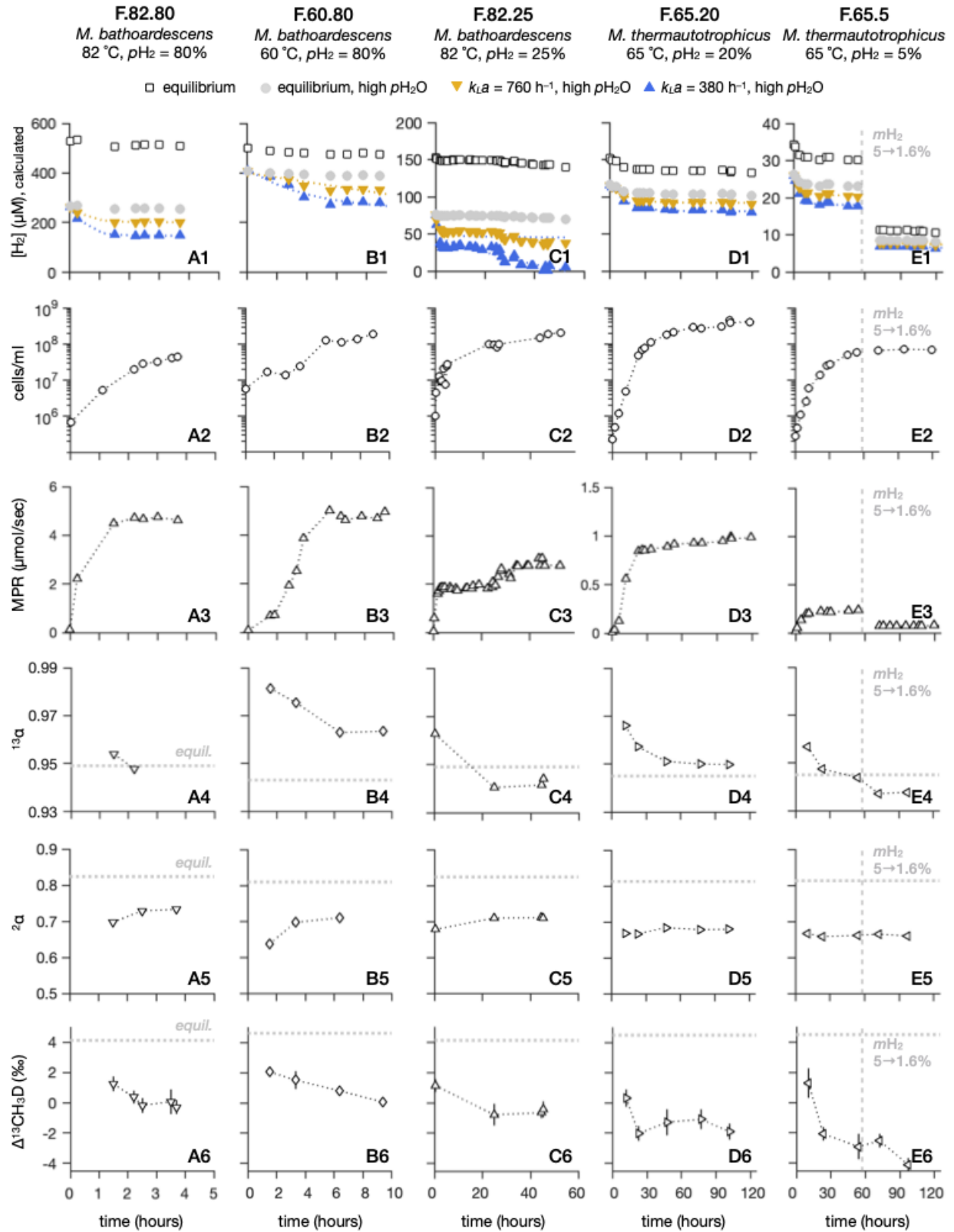


975

976 **Figure 1**

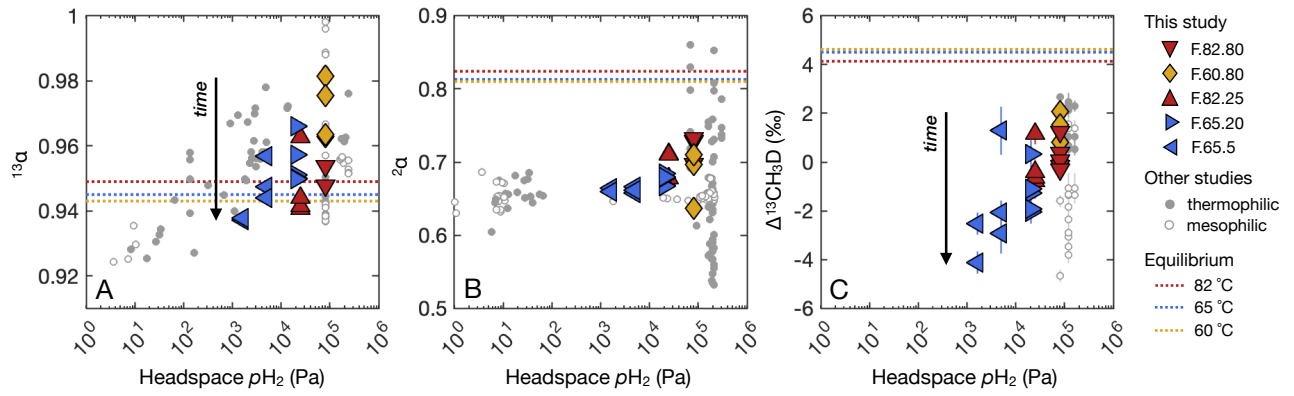


977
978 **Figure 2**



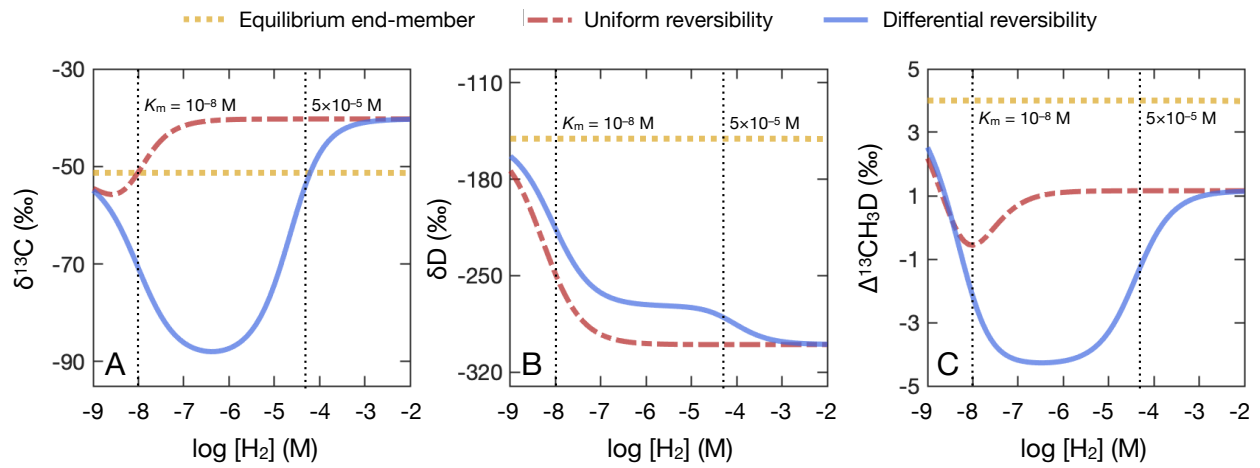
979
980
981

Figure 3

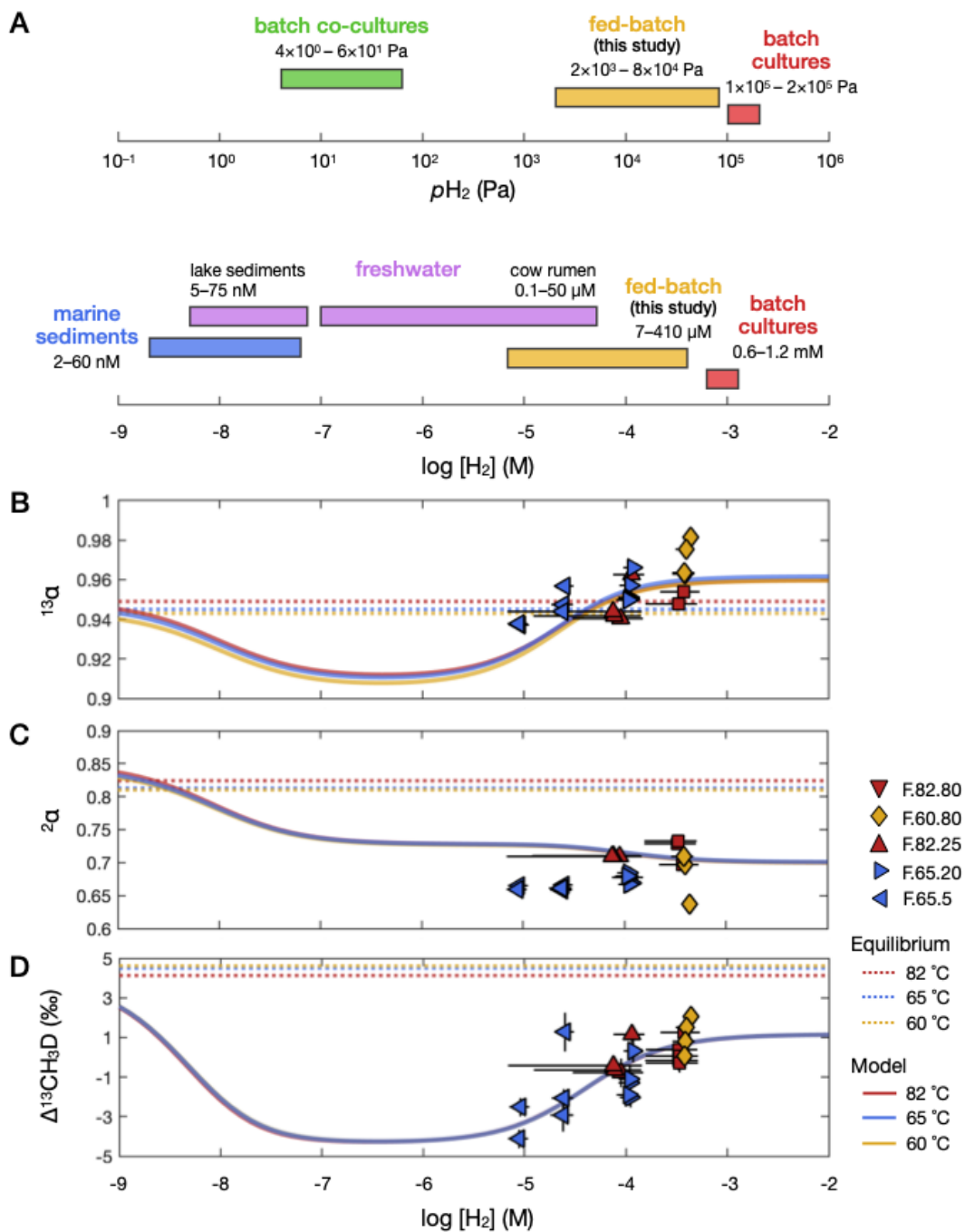


982
983 **Figure 4**

984
985



986
987
988 **Figure 5**



989

990 **Figure 6**

Supplementary Material

Combined carbon, hydrogen, and clumped isotope fractionations reveal differential reversibility of hydrogenotrophic methanogenesis in laboratory cultures

Jeemin H. Rhim^{a,1,*} and Shuhei Ono^a

^a *Department of Earth, Atmospheric and Planetary Sciences, Massachusetts Institute of Technology, Cambridge, MA 02139, USA. jrhim@alum.mit.edu (J. H. Rhim), sono@mit.edu (S. Ono)*

¹ *Present address: Department of Earth Sciences, Dartmouth College, Hanover, NH 03755, USA*

** Corresponding author: jrhim@alum.mit.edu*

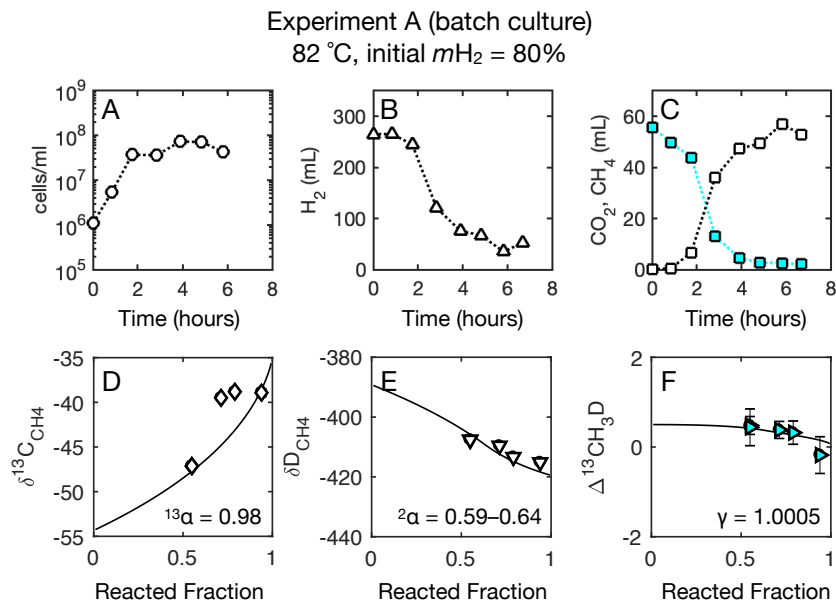


Figure S1. Temporal changes in cell density, headspace gases, and estimates of isotope fractionation factors during a batch culture experiment (Experiment B.82). *Methanocaldococcus bathoardescens* was grown at 82 °C and 80% H_2 . Notations for symbols: open circle (cell density; cells/mL), open up-pointing triangle (H_2 ; mL), filled squares (CO_2 ; mL), open squares (CH_4 ; mL), open diamonds ($\delta^{13}C_{CH_4}$; ‰), open down-pointing triangles (δD_{CH_4} ; ‰), and filled right-pointing triangles ($\Delta^{13}CH_3D$; ‰). The $\delta^{13}C_{CO_2}$ of the source CO_2 was -35% , and the δD_{H_2O} of the source water was -45% .

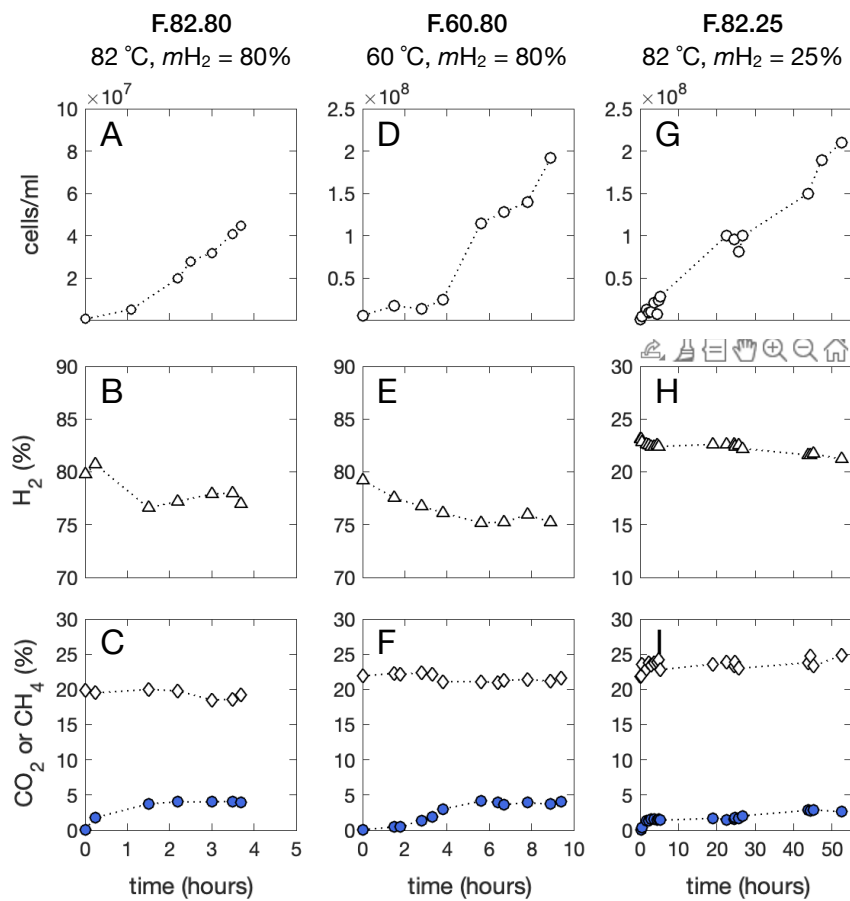


Figure S2. Temporal changes in cell density and headspace mixing ratios during fed-batch incubations of *Methanocaldococcus bathoardescens*. Experiment F.82.80 (panels A–C) was conducted at 82 °C and 80% H₂; Experiment F.60.80 (panels D–F) at 60 °C and 80% H₂; and Experiment F.82.25 (panels G–I) at 82 °C and 25% H₂. Notations for symbols: open circle (cell density; cells/ml), open up-pointing triangle (H₂; %), open diamonds (CO₂; %) and filled circles (CH₄; %). Note that timescales are different among experiments.

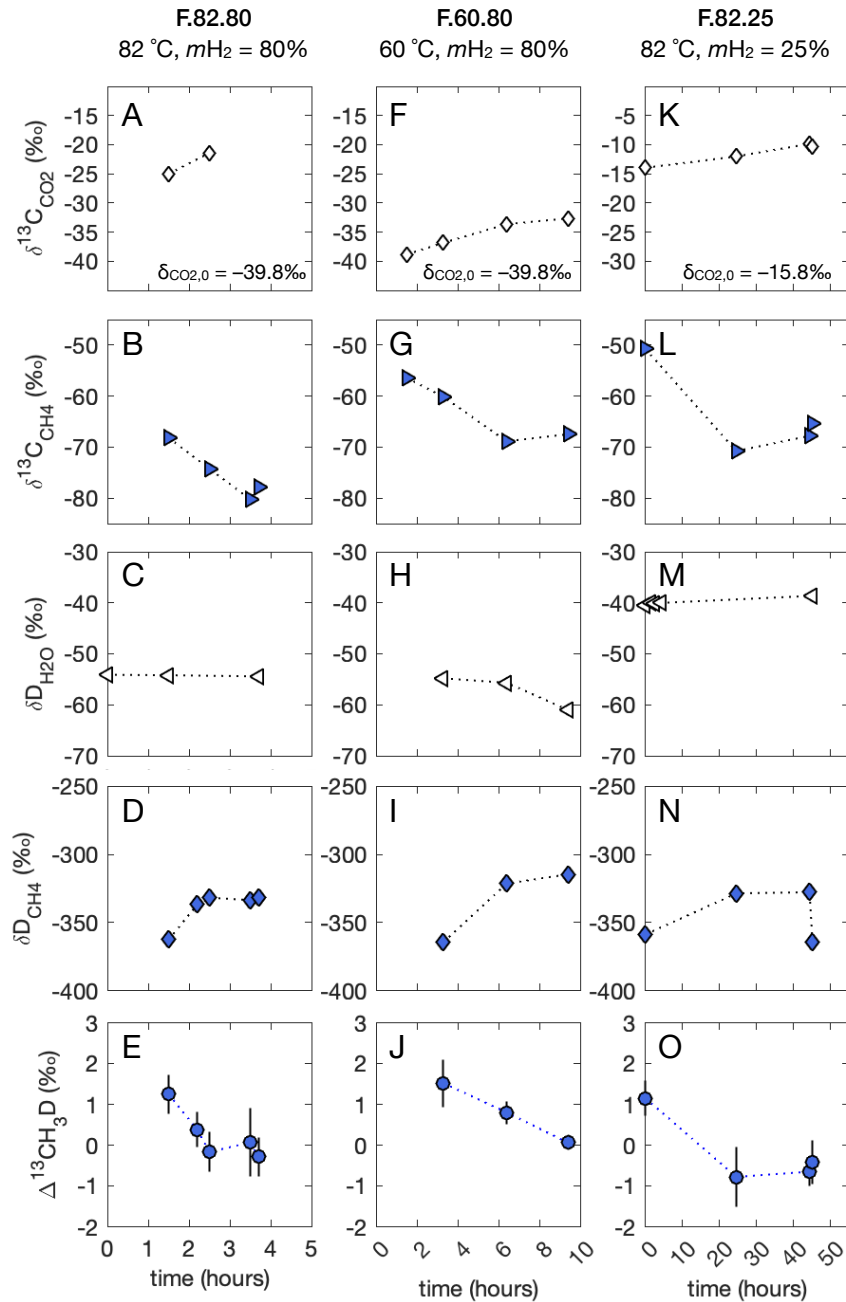


Figure S3. Temporal changes in bulk and clumped isotopologue ratios during fed-batch incubations of *Methanocaldococcus bathoardescens*. Experiment F.82.80 (panels A–E) was conducted at 82 °C and 80% H₂; Experiment F.60.80 (panels F–J) at 60 °C and 80% H₂; and Experiment F.82.25 (panels K–O) at 82 °C and 25% H₂. Notations for symbols: open diamonds (δ¹³C_{CO₂}; ‰), filled right-pointing triangles (δ¹³C_{CH₄}; ‰), open left-pointing triangles (δD_{H₂O}; ‰), filled diamonds (δD_{CH₄}; ‰) and filled circles (Δ¹³CH₃D; ‰). δ¹³C_{CO₂,0} values in panels A, F and K are the carbon isotopic compositions of CO₂ measured upstream. Note that timescales are different among experiments.

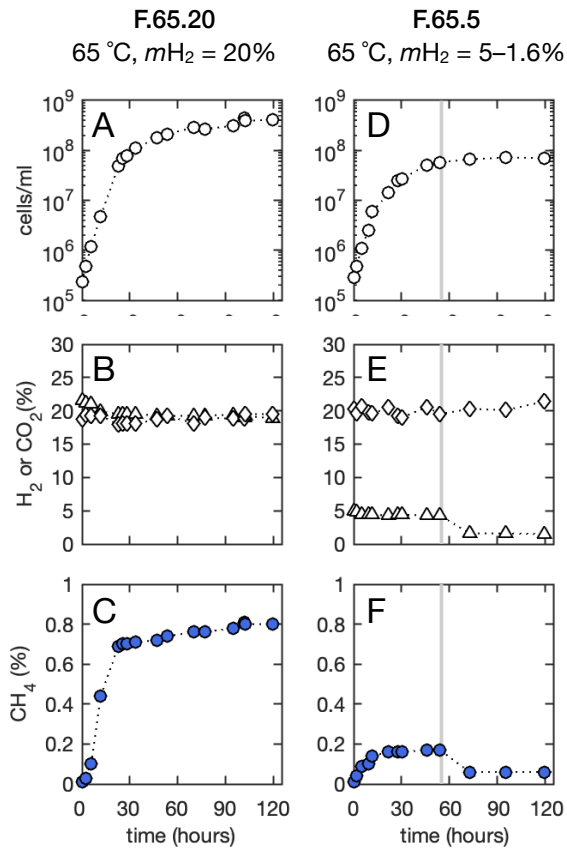


Figure S4. Temporal changes in cell density and headspace mixing ratio during fed-batch incubations of *Methanothermobacter thermaulithotrophicus*. Experiment F.65.20 (panels A–C) was conducted at 65 °C and 20% H₂ and Experiment F.65.5 (panels D–F) at 65 °C and 5% to 1.6% H₂. After 55 hours (grey vertical line, panels D–F), *x*H₂ was switched from 5% to 1.6%. Notations for symbols are as follow: open circles (cell density; cells/ml), open triangles (H₂; %), open diamonds (CO₂; %) and filled circles (CH₄; %).

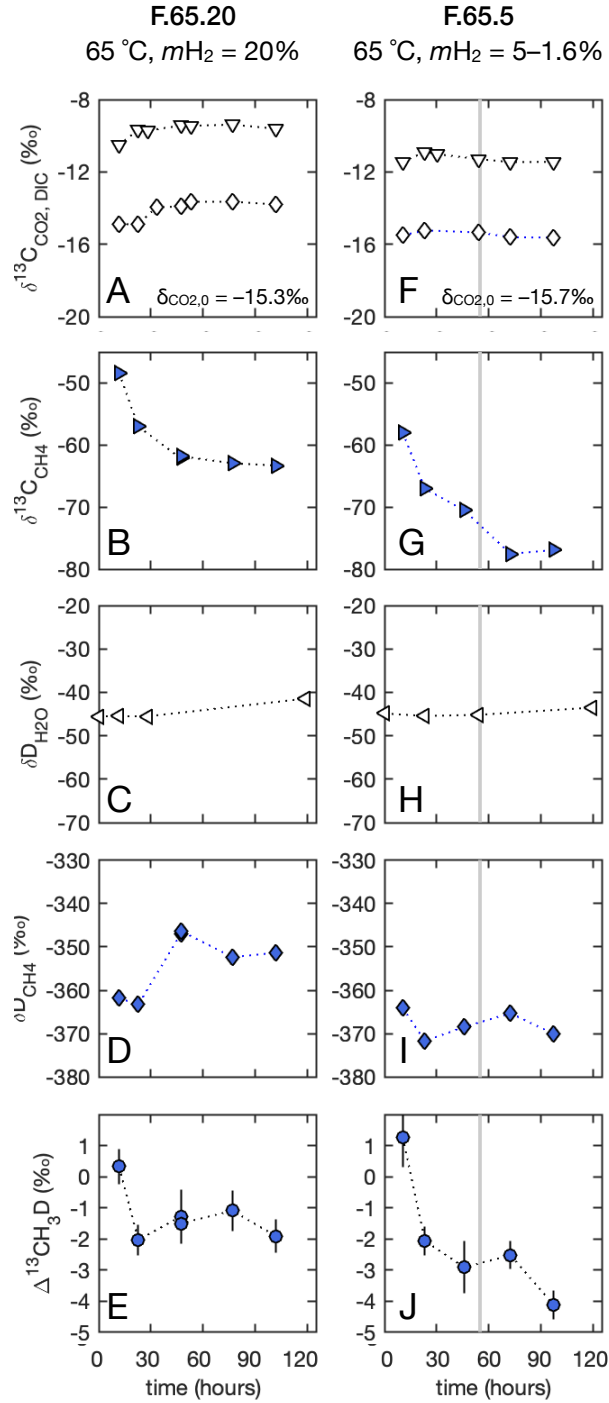


Figure S5. Temporal changes in bulk and clumped isotopologue ratios during fed-batch incubations of *Methanothermobacter thermautolithotrophicus*. Experiment F.65.20 (panels A–E) was conducted at 65 °C and 20% H₂. Experiment F.65.5 (panels F–J) at 65 °C and 5% to 1.6% H₂. After 55 hours (grey vertical line, panels D–F), xH₂ was switched from 5% to 1.6%. Notations for symbols: open down-pointing triangles ($\delta^{13}\text{C}_{\text{DIC}}$; ‰), open diamonds ($\delta^{13}\text{C}_{\text{CO}_2}$; ‰), filled right-pointing triangles ($\delta^{13}\text{C}_{\text{CH}_4}$; ‰), open left-pointing triangles ($\delta\text{D}_{\text{H}_2\text{O}}$; ‰), filled diamonds ($\delta^{13}\text{C}_{\text{CH}_4}$; ‰) and filled circles ($\Delta^{13}\text{CH}_3\text{D}$; ‰). $\delta^{13}\text{C}_{\text{CO}_2,0}$ values in panels A, F and K are the carbon isotopic compositions of CO₂ measured upstream.

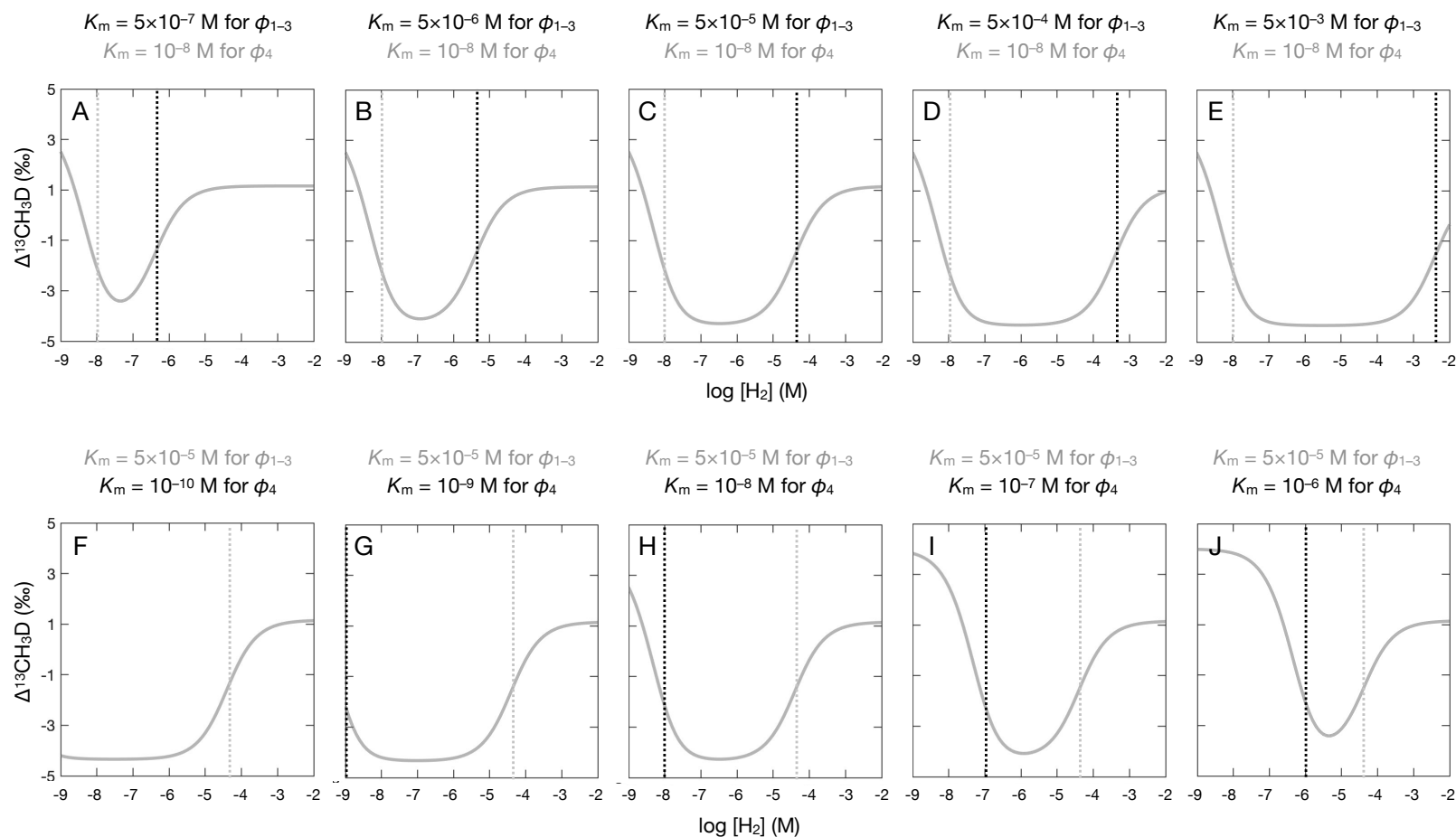
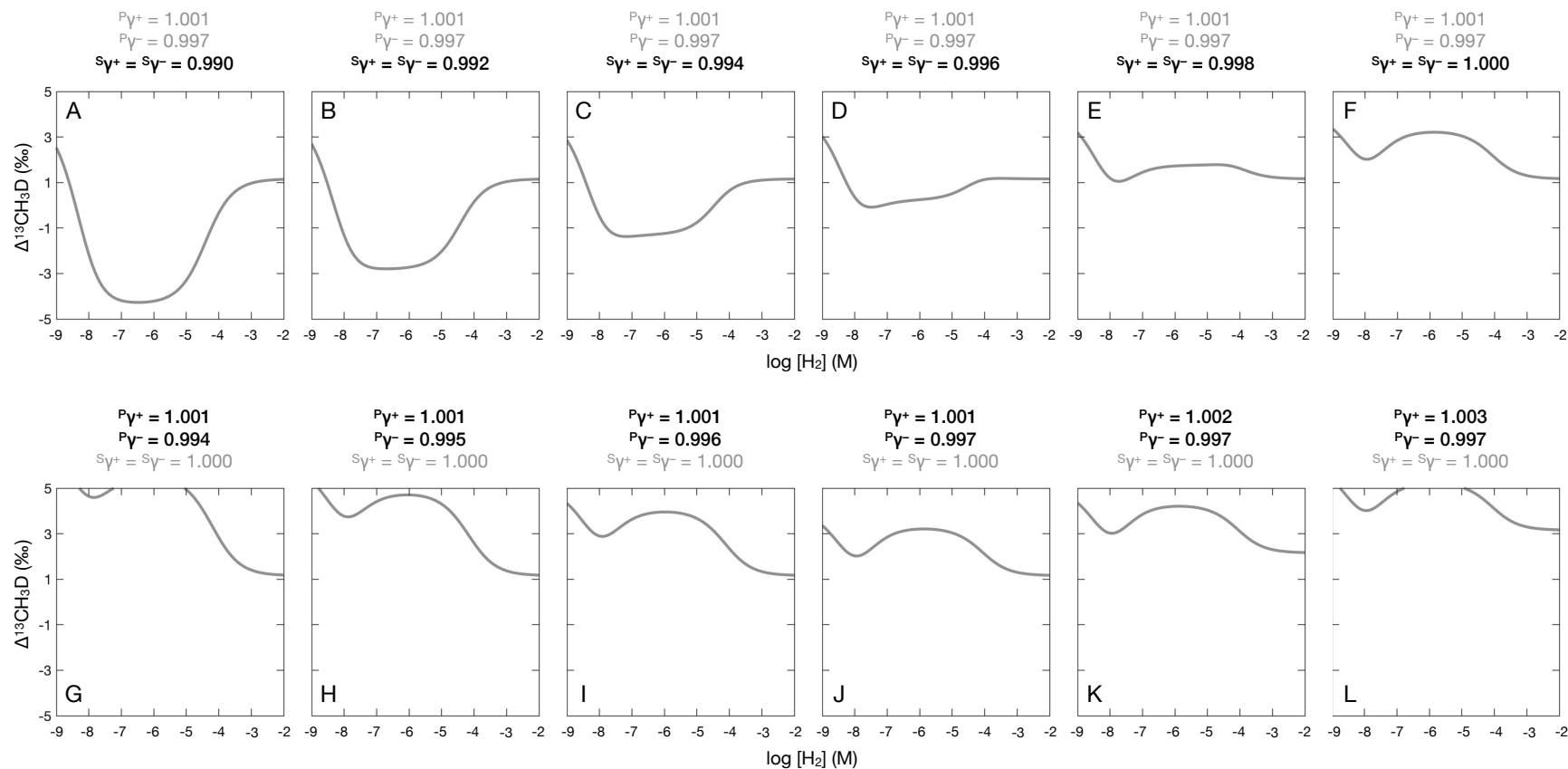


Figure S6. Modeled clumped isotopologue compositions ($\Delta^{13}\text{CH}_3\text{D}$) of methane produced via hydrogenotrophic methanogenesis with different effective half-saturation constants (K_m) for the differential reversibility scenario in **Error! Reference source not found.C**. The top row (panels A–E) shows $\Delta^{13}\text{CH}_3\text{D}$ profiles with the same K_m value for the fourth H-addition step ($K_m = 10^{-8}$ M for ϕ_4 , where ϕ represents metabolic reversibility) and different K_m values for the first three H-addition steps ($K_m = 5 \times 10^{-7}$ to 5×10^{-3} M for ϕ_{1-3}). The bottom row (panels F–J) shows $\Delta^{13}\text{CH}_3\text{D}$ profiles with the same K_m value for the first three H-addition steps ($K_m = 5 \times 10^{-5}$ M for ϕ_{1-3}) and different K_m values for the first three H-addition steps ($K_m = 10^{-10}$ to 10^{-6} M for ϕ_4). Note that panels C and H are the same $\Delta^{13}\text{CH}_3\text{D}$ profile for the differential reversibility scenario in **Error! Reference source not found.C**. See section **Error! Reference source not found.** for more details about the model



KIE values used in the isotopologue flow network model

We assign a KIE for the forward reaction (α^+) and derive the reverse KIE (α^-) that maintains internal consistency, and vice versa, using α^{eq} values:

$$\alpha^{eq} = \frac{\alpha^-}{\alpha^+} \quad (\text{Eqn. S1})$$

For deuterated isotopologues, both primary ($^P\alpha$) and secondary ($^S\alpha$) KIEs are considered in the model (Table S1). Primary KIEs apply when a C–D bond is directly broken or formed during a reaction, whereas secondary KIEs apply when one or more C–D bond(s) is(are) transferred from a reactant to a product while a C–H bond is directly broken or formed instead. The following equations define the parameters reported in Table S1:

$$^{2,P}\alpha^{eq} = \frac{^{2,P}\alpha^-}{^{2,P}\alpha^+} \quad (\text{Eqn. S2})$$

$$^{2,S}\alpha^{eq} = \frac{^{2,S}\alpha^-}{^{2,S}\alpha^+} \quad (\text{Eqn. S3})$$

where the numeric superscript on the top left corner (e.g., 2) denotes the type of isotope system (e.g., 2 for hydrogen); the alphabetic superscripts, “P” and “S,” denote primary and secondary KIEs, respectively; and the “+” and “–” superscripts on the top right corner denote forward and backward reactions, respectively (Table S1).

KIEs for clumped isotopologues follow the rule of geometric mean (Bigeleisen, 1955). For example, the KIE for $^{13}\text{CH}_3\text{D}$ is approximately the product of KIEs for $^{13}\text{C}/^{12}\text{C}$ and D/H. The primary KIE for clumped isotopologues ($^P\gamma$) is defined as the deviation from this product (Wang et al., 2015). Similar to α values, the backward ($^P\gamma^-$) clumped isotopologue KIE is derived by assigning a forward value ($^P\gamma^+$) and using equilibrium values ($^P\gamma^{eq}$; 1.004 at 82 °C):

$$P\gamma^{eq} = \frac{P\gamma^-}{P\gamma^+} \quad (\text{Eqn. S4})$$

$$S\gamma^{eq} = \frac{S\gamma^-}{S\gamma^+} \quad (\text{Eqn. S5})$$

Table S1. $^{13}\text{C}/^{12}\text{C}$ and D/H isotope fractionation factors used as input parameters for the isotopologue flow network model in this study. See **Error! Reference source not found.** for model description. Values shown in italic are prescribed fractionation factors, and those in non-italic are derived values using Eqn. S2 and S3.

Reaction	$^{13}\alpha^{eq}$	$^{13}\alpha^+$	$^{13}\alpha^-$	$^{2,P}\alpha^{eq}$	$^{2,P}\alpha^+$	$^{2,P}\alpha^-$	$^{2,S}\alpha^{eq}$	$^{2,S}\alpha^+$	$^{2,S}\alpha^-$
1	0.9853 ^a	<i>0.9600^b</i>	0.9743	0.9077 ^a	<i>0.7^b</i>	0.7712	n.a.	n.a.	n.a.
2	0.9862 ^a	<i>0.9600^b</i>	0.9734	0.9609 ^a	<i>0.7^b</i>	0.7285	1.0587 ^a	<i>0.84^b</i>	0.7934
3	0.9758 ^a	<i>0.9600^b</i>	0.9838	0.8779 ^a	<i>0.7^b</i>	0.7974	0.9136 ^a	<i>0.84^b</i>	0.9194
4	1.0005 ^a	<i>0.9600^b</i>	0.9595	0.8494 ^a	<i>0.7^b</i>	0.8241	0.9675 ^a	<i>0.84^b</i>	0.8682

n.a., not applicable; ^aGropp, Iron and Halevy (2020), 82 °C; ^bScheller et al. (2013).

Table S2. Clumped isotope fractionation factors used as input parameters for the isotopologue flow network model in this study. See **Error! Reference source not found.** for model description. Values shown in italic are prescribed fractionation factors, and those in non-italic are derived values using Eqn. S4 and S5.

Reaction	$P\gamma^{eq}$	$P\gamma^+$	$P\gamma^-$	$S\gamma^{eq}$	$S\gamma^+$	$S\gamma^-$
1	1.004	<i>0.998</i>	0.994	n.a.	n.a.	n.a.
2	1.004	<i>0.998</i>	0.994	1.000	<i>0.991</i>	0.991
3	1.004	<i>0.998</i>	0.994	1.000	<i>0.991</i>	0.991
4	1.004	<i>0.998</i>	0.994	1.000	<i>0.991</i>	0.991

n.a., not applicable